

Accepted Manuscript

Effects of graphene nano-platelets (GNPs) on the microstructural characteristics and textural development of an Al-Mg alloy during friction-stir processing

F. Khodabakhshi, M. Nosko, A.P. Gerlich



PII: S0257-8972(17)31276-8
DOI: <https://doi.org/10.1016/j.surfcoat.2017.12.045>
Reference: SCT 22963
To appear in: *Surface & Coatings Technology*
Received date: 3 October 2017
Revised date: 28 November 2017
Accepted date: 19 December 2017

Please cite this article as: F. Khodabakhshi, M. Nosko, A.P. Gerlich , Effects of graphene nano-platelets (GNPs) on the microstructural characteristics and textural development of an Al-Mg alloy during friction-stir processing. The address for the corresponding author was captured as affiliation for all authors. Please check if appropriate. Sct(2017), <https://doi.org/10.1016/j.surfcoat.2017.12.045>

This is a PDF file of an unedited manuscript that has been accepted for publication. As a service to our customers we are providing this early version of the manuscript. The manuscript will undergo copyediting, typesetting, and review of the resulting proof before it is published in its final form. Please note that during the production process errors may be discovered which could affect the content, and all legal disclaimers that apply to the journal pertain.

Effects of graphene nano-platelets (GNPs) on the microstructural characteristics and textural development of an Al-Mg alloy during friction-stir processing

F. Khodabakhshi^{a,*}, M. Nosko^b, A.P. Gerlich^c

^aSchool of Metallurgical and Materials Engineering, College of Engineering, University of Tehran,
P.O. Box: 11155-4563, Tehran, Iran

^bInstitute of Materials and Machine Mechanics, Slovak Academy of Sciences, Dúbravská cesta
9/6319, 845 13, Bratislava, Slovak Republic

^cDepartment of Mechanical and Mechatronics Engineering, University of Waterloo, Waterloo, ON,
Canada

*Corresponding author: Tel: +98 (21) 8208 4127, Fax: +98 (21) 8800 6076; E-mail:

fkhodabakhshi@ut.ac.ir, farzadkhodabakhshi83@gmail.com, fkhodaba@uwaterloo.ca (F.
Khodabakhshi)

Abstract

The aim of this research is to characterize the unique microstructural features of Al-matrix nanocomposites reinforced by graphene nano-platelets (GNPs), fabricated by multi-pass friction-stir processing (FSP). During this process, secondary phase GNPs were dispersed within the stir zone (SZ) of an AA5052 alloy matrix, with a homogenous distribution achieved after five cumulative passes. The microstructural characteristics and crystallographic textures of different regions in the FSPed nanocomposite, *i.e.*, base metal (BM), heat affected zone (HAZ), thermo-mechanical affected zone (TMAZ), and SZ, were evaluated using electron back scattering diffraction (EBSD) and transmission electron microscopy (TEM) analyses. The annealed BM consisted of a nearly random crystal orientation distribution with an average grain size of 10.7 μm . The SZ exhibited equiaxed recrystallized grains with a mean size of 2 μm and a high fraction of high-angle grain boundaries (HAGBs) caused by a discontinuous dynamic recrystallization (DDRX) enhanced by pinning of grain boundaries by GNPs. The sub-grains and grain structure modification within the HAZ and TMAZ regions are governed by dislocation annihilation and reorganization in the grain interiors/within grains which convert low-angle to high-angle grain boundaries via dynamic recovery (DRV). The FSP process and incorporation of GNPs produced a pre-dominantly $\{100\} \langle 100 \rangle$ cube texture component in the SZ induced by the stirring action of the rotating tool and hindering effect of nano-platelets. Although, a very strong $\{112\} \langle 110 \rangle$ simple shear texture was found in the HAZ and TMAZ regions governed by additional heating and deformation imposed by the tool shoulder. These grain structure and texture features lead to a hardness and tensile strength increases of about 55% and 220%, respectively.

Keywords: Al-Mg alloy; Friction-stir processing; Graphene; Microstructure; Texture

1. Introduction

Metal matrix nanocomposites may be considered multifunctional materials owing to their exceptional physical and mechanical properties which can be tailored to meet the requirements of various industrial applications [1]. Therefore, development of these materials and their related technologies for design and manufacturing have involved highly developed processing and characterization techniques in materials science and engineering [2]. Aluminum and its alloys have been broadly employed in various fields of industrial applications such as aeronautical, aerospace, automotive and electronic packaging, given their superior properties including low density, high strength, good workability, corrosion resistance, and good weldability [3]. However, application of these metals and alloys is restricted by low hardness and wear resistance [4]. Enhancing the mechanical strength of aluminum alloys will always be very important and challenging for structural design [5]. Embedding the reinforcing secondary phase nano-materials into an Al-matrix to refine a microstructure and hinder dislocation sliding with fabrication of Al-matrix nanocomposite is one potential way to improve mechanical performance of aluminum alloys [6, 7]. Processing of these materials is mainly based on powder metallurgy (PM) route and molten metal technology, or in more recent years by using severe plastic deformation (SPD) [8]. Several methods have been introduced for this aim, such as; mechanical alloying (MA) [7, 9], pressurized squeeze casting [10], and accumulative roll bonding (ARB) [11].

Recently, friction-stir processing (FSP) has attracted much attention as a surface modification technology, and is based on the friction-stir welding (FSW) technique [12, 13]. FSP is a very effective technique to produce fine-grained metals exhibiting superplasticity, to homogenize the powder metallurgy processed and cast materials, and to fabricate metal-matrix nanocomposites [14]. In this process, a non-consumable rotating tool is plunged into the surface to be modified. The local temperature of the processed material increases up to the

range of 0.6 to 0.9 T_m depending on the processing parameters, by localized heating due to friction between the rotating tool and the workpiece, and severe plastic deformation of material around the rotating tool [15]. By traversing the rotating tool along the processing direction, the plasticized material is forged from leading to trailing edge [15]. Although, a secondary circular motion is imposed as well around the longitudinal weld axis due to the tool stirring action combined with extrusion flow [16]. As a result, significant microstructural modifications occur during the FSP process due to imposing intense plastic deformation to the material in the processed zone, beside of mixing and thermal exposure [17]. Recently, FSP has been successfully applied to produce surface Al-matrix nanocomposites reinforced with various nano-particles (including SiC [18-20], Al_2O_3 [21-23], B_4C [24, 25], TiC [26], fullerene [27], SiO_2 [28, 29], TiO_2 [30-32], TiB_2 [33], intermetallics [34]) or nano-tubes (including single- [35] and multi-wall carbon nano-tubes (CNTs) [36, 37]).

Graphene is a sp^2 -hybridized two-dimensional single-atom thick-layer structure of graphite which has attracted particular interests in the recent years, considering its unique thermal, electrical, and mechanical properties [38]. It can be produced via several methods based on thermal or chemical reduction of graphene oxide (GO), but usually created from the Hummer's approach [39]. Synthesis of this new carbon-based nano-material in the form of sheet is preferred, since this can considerably outperform the properties of CNTs in many respects [40, 41]. Graphene nano-platelets (GNPs) exhibit a theoretical strength of about 1060 GPa, which is more than one hundred times higher than structural steel [42]. These mechanical properties associated with graphene have garnered great interest in incorporating these nano-platelets within metal matrixes to form nanocomposites with significantly enhanced mechanical performance. Various liquid- and solid-state processing techniques have been employed to disperse the GNPs within the metal matrixes for fabricating the high

strength nanocomposites [43-46].

Although there is great potential to enhance properties using graphene, aggregation of nano-platelets and weak bonding at the interfaces with the matrix have been found to be critical in limiting the key mechanical properties. Therefore, it remains a great challenge to produce metal-matrix nanocomposites by incorporating well dispersed GNPs. Also, another major challenge in using carbon-based nano-materials as a reinforcement is preventing damage to their intrinsic structure during processing [47]. To the author's best knowledge, very limited research about the application of FSP process to fabricate graphene reinforced metal-matrix nanocomposites have been reported so far [48, 49]. In the first attempt to fabricate an Mg-based metal matrix nanocomposite by Chen et al. [48], graphene nano-platelets were homogeneously dispersed inside a magnesium alloy plate with a combination of liquid-state ultrasonic vibration and solid-state friction-stirring, and this led to a considerable enhancement of mechanical properties. Thereafter, limited research was reported by Jeon et al. [49] on the physical and mechanical properties of aluminum-matrix nanocomposites reinforced by graphene oxide (GO) particles prepared by friction-stir processing. Therefore, more studies on metal-matrix nanocomposites reinforced with graphene by FSP process are worthwhile and interesting. In order to contribute to developing a new kind of structural-functional integrated composite material, the objective of the work reported in this study was to characterize an Al-matrix nanocomposite reinforced with GNPs fabricated by friction-stir processing.

A variety of microstructural features and textural components can develop in the surrounding material due to the stirring action of the rotating tool, and this will control the mechanical performance of the friction-stir processed materials [50]. According to the literature [51], the predominant deformation mode during the FSP process is expected to be simple shear extrusion which leads to the formation of shear textural components defined in the terms of

crystallographic planes and directions aligned along the shear planes and directions. In previous studies [52-55], it was proposed that various FCC shear texture components arise (including $\{110\} \langle 001 \rangle$ and $\{114\} \langle 221 \rangle$ in aluminum alloys; $\{1\bar{1}\bar{1}\} \langle 110 \rangle$, $\{\bar{1}12\} \langle 110 \rangle$, $\{001\} \langle 110 \rangle$, and well-defined $\{11\bar{2}\} \langle 111 \rangle$ in steels) during FSP of metals and alloys depending on the processing conditions and the examined material. In the case of FSP of Al-matrix nanocomposites, only limited works have been performed by Khodabakhshi et al. [56, 57] analyzing the crystallographic texture evolution in an Al-Mg alloy reinforced by incorporation of TiO₂ nanoparticles during FSP process. To-date, there is no report on the effects of graphene nano-platelets (GNPs) on the crystallographic textural developments during FSP process. It has been demonstrated that various dynamic restoration mechanisms control the microstructural refinements within the stir zone (SZ) during FSP process, and these subsequently determine the formation of textures reflecting the compressive and shear deformation modes induced by the shoulder and pin of rotating tool [58]. Despite these correlations, microstructure development during FSP of metal-matrix nanocomposites is not well understood, although this is essential in optimizing the process and manufactured products.

Aside from grain refinement during FSP, the grain boundary character can be modified based on the coincidence site lattice (CSL) geometric model, in which the arrangement of atoms at the boundary in a super-lattice consisting of coincidence sites, grain boundaries can be categorized into three different types [59, 60]; (i) low angle grain boundaries (LAGBs) with misorientation angle less than 15°, (ii) low Σ CSL boundaries with $3 \leq \Sigma \leq 29$ (i.e., $\Sigma 3^n$ and $n \geq 1$), and (iii) general boundaries. The Σ value is defined as the ratio of CSL atoms to the standard unit-cell atoms at the boundary [59]. Recently, it was shown the low Σ CSL boundaries have an impact on the physical and mechanical properties of materials, and can be

regarded as “low-energy” or “special boundaries” owing to their excellent atomic fit and crystallographic match with the lattice [59, 60]. Also, these boundaries offer great resistance to inter-granular corrosion and thus can promote significant improvements in creep resistance and stress-corrosion cracking (SCC) [59]. However, there is no report on the effects of GNPs as a secondary phase reinforcing agent on the promotion of CSL boundaries structure as induced by FSP modification within the aluminum matrix.

Therefore, in the current work, electron back scattered diffraction (EBSD) analysis was used to interpret the crystallographic texture within different regions of FSP synthesized Al-Mg/GNPs nanocomposite, including the base metal (BM), heat affected zone (HAZ), thermo-mechanical affected zone (TMAZ), and SZ. The goal is to deduce the material flow during FSP process, while the details of the restoration mechanisms for the processed nanocomposite are studied using transmission electron microscopy (TEM) analysis techniques.

2. Materials and methods

2.1 Raw materials

The aluminum-magnesium alloy used for composite fabrication was AA5052 series with a chemical composition of 97Al-2.23Mg-0.292Fe-0.163Cr-0.147Si-0.114Mn-0.0077Zn-0.0065Cu (in wt. %) and thickness of 5 mm, supplied by Arak Aluminum Company (Arak, Iran). This sheet was cut to small samples with a cross-sectional area of $210 \times 70 \text{ mm}^2$ and was annealed at a temperature of 500 °C for 2 hr followed by water quenching. Graphene nano-platelets (GNPs) in the form of powder were used as the reinforcement, and were obtained from US Nano Company (US NANO, USA) with product number of US1073. Transmission electron microscopy (TEM) images of the graphene base material powder are presented in Fig. 1. The average thickness and diameters of an initial single platelet were about 20 nm and 2 μm , respectively.

2.2 Friction-stir processing

To prepare the Al-matrix nanocomposite using these materials, FSP was employed first on a 1.2 mm deep groove with a cross-section of $210 \times 3.5 \text{ mm}^2$ machined in the middle of the Al-Mg sheet, where the GNP powder was pre-placed. After the powder was introduced into the groove and compacted by hand, the open top surface was closed by employing one capping pass. For this aim, a modified milling machine and a cylindrical tool (with no pin) with a diameter of 12 mm were used, which was made from H13 steel. This capping pass was performed using a tool rotational speed (w) of 1250 rpm and a traverse velocity (v) of 25 mm/min to minimize the machine vibrations. Following this step, the embedded GNPs were dispersed within the Al-Mg matrix by applying FSP passes with a conventional tool. Conventional tool consists of a concave-profiled shoulder with diameter of 18 mm and a M5 threaded cylindrical pin with a length of 4 mm and a diameter of 5 mm, and is also made from H13 hot die steel. This was used to perform FSP using parameters of $w=1200$ rpm and

$v=100$ mm/min up to five subsequent passes with 100% overlap, keeping the directions of rotation and traverse movements the same between passes. Also, a tool tilt angle of 3 degrees with respect to the vertical axis was kept during processing. By measuring the sample weight changing before and after FSP and also determining the SZ cross-sectional area by image analyzing, the amount of embedded GNPs was estimated about 3 vol%. In addition, the Al-Mg alloy was processed with the same parameters but without introducing GNPs powder, for the aim of comparison to the FSP synthesized composite.

2.3 Electron backscatter diffraction (EBSD) analysis

Electron backscatter diffraction (EBSD) analysis was performed to study microstructure within the Al-Mg-GNPs nanocomposites. Samples were cut perpendicular to the FSP direction using electrical discharge machining (EDM). Standard metallographic techniques involved mechanical grinding using SiC papers until 3000 grit size, followed by polishing using 1 μm diamond paste using an automatic grinding/polishing machine (FORCIPOL; Kemet International Ltd; UK) while keeping the vertical load at 20 N were used to prepare sample surface. Finishing step was done by chemo-mechanically polishing using an OPS (silica) suspension with average diameter of 25 nm (SiO_2 , US NANO, USA), with vertical force of 10 N for 45 minutes. To increase the indexing rate to over 90% during EBSD data collection, the surface of sample was further polished by cross-sectional ion milling (JEOL IB-19530CP Cross-Section Ion Polisher, Japan) up to about 2 hrs. The crystallographic studies were performed by using a field emission-scanning electron microscope (FEG-SEM, JEOL 7600F, Japan) equipped with an EBSD detector and analysis system (Oxford Instruments HKL Technology CHANNEL 5) operating at 10 keV. The step size for electron beam scanning was 1 μm for base metal and 0.25 μm for HAZ and weld over an indexing area of 250 $\mu\text{m} \times 250 \mu\text{m}$. The analysis of obtained crystallographic orientation data was expressed in the terms of EBSD microstructural maps and textural plots. Tango software was

utilized to plot orientation, grain boundary, phase, and pattern quality maps from the EBSD analysis data. Also, automatic grain size measurement and subset analysis was performed using this software as well. To plot (inverse) pole figures from EBSD orientation and misorientation data, Mambo software was used, while Salsa software was employed to plot 2D and 3D orientation distribution functions (ODFs).

2.4 Transmission electron microscopy (TEM) study

Thin foils were prepared for TEM analysis with cross-sectional area of $10 \times 10 \text{ mm}^2$ and thickness of $200 \text{ }\mu\text{m}$, which were extracted from the center of the SZ region by EDM. Subsequently, foil was mechanically grinded and polished from two sides to reduce its thickness down to $50 \text{ }\mu\text{m}$. A 3 mm diameter disk was punched from the thin foil and thinned further using a PIPS II ion milling machine (Gatan, USA) set at a voltage of 5 keV until perforation. The microstructural features were then characterized using a TEM (JEOL 2000FX, Japan) operating at voltage of 200 keV . More than one hundred sub-grains and secondary phase nano-particles were evaluated to determine their average sizes.

2.5 Mechanical testing

To determine mechanical performance of the processed Al-Mg-GNPs nanocomposites, indentation and tensile testing were performed. Samples for tensile test were prepared with a gauge length of 32 mm and a width of 6 mm according to the ASTM E8M Standard [61], which were extracted along the FSP direction by EDM cutting, such that the gauge length was located within the middle of the SZ with a thickness of about 3 mm (smaller than the thickness of sheet and FSP modified region). Thereafter, surfaces of the prepared tensile coupons were mechanically grinded with using SiC papers up to 1000 grit to remove the re-melted layer of EDM process before testing. Longitudinal tensile tests were conducted on the prepared coupons with using a Hounsfield Universal Tensile Testing Machine (Model H10K, Tinius Olsen, USA) at room temperature and initial strain rate of $5 \times 10^{-4} \text{ sec}^{-1}$. To examine

the repeatability of the measured tensile data, tests were repeated three times for each condition and average values of the key tensile properties (Young's modulus, yield stress, ultimate-tensile strength, fracture stress, and elongation) are reported. Indentation Vickers micro-hardness measurements were performed across thickness of the FSPed materials according to the ASTM E 384-99 Standard [62], to determine the average hardness of different regions (BM, HAZ, TMAZ, and SZ). These measurements were performed along a straight line of 2 mm below the top surface across the different regions (distance 0.5 mm from the center of SZ) with 0.25 mm intervals by using a computerized Bohler micro-hardness tester (Bohler, Germany) and average values for each region calculated and reported. For testing at each point, a load of 250 g was applied for a holding time of about 15 sec.

3. Results and discussion

3.1 Microstructural evolutions by EBSD analysis

The cross-sections of the FSPed Al-Mg alloy and Al-Mg-GNPs nanocomposite samples are shown in Fig. 2a and 2b, respectively. The material flow could be easily distinguished based on the contrast arising from the graphene distribution in the nanocomposite sample (see Fig. 2b). A SZ with a trapezoidal shape and onion ring structure is formed during FSP process. As previously proposed [27], convectional material flow (with an elliptical path across the thickness section of SZ from bottom to top mainly induced by the rotating shoulder effect) during friction stirring before consolidation process is responsible for the formation of this onion ring structure. Meanwhile, for the FSPed Al-Mg alloy in Fig. 2a this banded onion ring flow pattern structure would be very fine considering the strong contrast derived from the different grain structures. An FE-SEM micrograph from the cross-section of this processed nanocomposite after ion milling illustrates the macro- and microstructures of different regions in Fig. 3. The locations of areas for EBSD analysis from the BM, HAZ &

TMAZ, and SZ regions across the thickness section as combined with the corresponding EBSD maps are indicated on this image. EBSD was used to characterize the grain boundaries and preferred crystallographic orientations. Maps from the SZ region of the processed Al-Mg alloy and BM, HAZ/TMAZ, and SZ regions across the processed nanocomposite are presented in Figs. 4 and 5, respectively. Figure 5 indicates the low-angle grain boundary (LAGBs) with a misorientation angle in the range of 3° to 15° (white lines), and high-angle grain boundaries (HAGBs) with misorientations higher than 15° (red lines). Histograms of the grain size distributions are plotted in Fig. 6. Figures 7 and 8 represent the maps and fraction curves from the recrystallized, substructured, and deformed grains within the BM, HAZ/TMAZ and SZ. The main microstructural statistics are summarized in Table 1. The annealed BM exhibited a coarse bi-modal grain structure with an average size of $10.7 \mu\text{m}$, with a high fraction of recrystallized grains (96%), and a fraction of HAGBs of around 89%. In the SZ of the processed Al-Mg alloy, the result of dynamic recrystallization (DRX) caused by frictional thermal exposure and intense plastic deformation during FSP process led to formation of a fine recrystallized equiaxed grain structure with the average size of $4.5 \mu\text{m}$ (see Fig. 4a). By incorporation of GNPs inside the SZ of processed nanocomposite, the grain structure refinement intensified, allowing a mean size of $2.1 \mu\text{m}$ and large fraction of HAGBs ($\sim 93\%$). The TMAZ is the transition zone between the SZ and HAZ regions which has experienced the combined thermal and deformation effects of the rotating shoulder action, which promoted formation of high substructured grains and low fraction of HAGBs. Figure 9 shows the distribution maps for these CSL boundaries at different regions of the processed nanocomposite. As reported in Table 1, after the FSP process, when GNPs are incorporated in the composite, the fraction of low Σ CSL boundaries at HAZ/TMAZ regions is increased, while the fraction in the SZ is decreased. Although, these fractions are still very low and only in the range of 2-6% of the total grain boundaries are detected in this region.

The quantitative fraction of each type of CSL boundary is presented in histograms in Fig. 10. It can be noted that new $\Sigma 3$, $\Sigma 9$, and $\Sigma 27$ boundaries are generated during FSP process following dynamic restoration mechanisms. As it is widely accepted [59, 60], these new boundaries can be formed due to atomic interactions associated with grain boundary migration phenomenon during DRX. However, when employing the FSP process with the addition of GNPs, more grains interfaced with these operating dynamic restoration mechanisms leads to the formation of higher fractions of low Σ CSL boundaries.

3.2 Sub-grains and ultra-fine grains by TEM analysis

Bright- and dark-field TEM images from the grain structure of the SZ in the FSPed Al-Mg-GNPs nanocomposite are presented in Fig. 11. Since TEM is a very local analysis method, various images in Figs. 11a-i illustrate the sub-grain structure at different regions and different magnifications to cover an average area inside the SZ as an indication for homogeneity of processed material. Moreover, the selected-area electron diffraction (SAED) spot pattern from the deformed and recrystallized Al-matrix is shown in Fig. 12a. Dark-field TEM image correspond to the indicated spot in Fig. 12 which showing a bright contrast from its related grain is demonstrated in Fig. 12b. In an overview from the substructure of the Al-matrix, a recrystallized fine equiaxed grain structure can be observed corresponding to the recrystallized SZ. The fine grains within the substructure consisted of HAGBs and little evidence of recovery structures are detected within the SZ. Even for ultra-fine grains shown in the images of Figs. 11a-b,f,g, the contrast due to tilting during TEM analysis does not indicate the presence of dislocation cell structures. As shown in the dark-field TEM image of Fig. 11d,i, sub-grains exhibit sharp boundaries with high diffraction contrast between neighbors. Also, interiors of ultra-fine grains are dislocation-free with sharp or clear boundaries (see Figs. 11f,g). A particular diffraction condition provided high contrast from the inclined grain boundaries is shown in Fig. 12b. It can be noted this grain consists of one

dominant orientation with some darker broad bands around it, indicating some tilting potentially due to long-range stress fields induced by the absorption of lattice dislocations [63]. These microstructural features observed by TEM analysis indicate that the grain structure within the SZ is highly clearly formed by the dynamic DRX mechanism at elevated temperature during FSP.

3.3 Restoration mechanisms

A very broad history about the dynamic restoration mechanisms responsible for microstructural refinements during FSW/FSP processes of Al-Mg alloys can be found with a literature survey [64-66]. The precise details regarding the dynamic restoration mechanisms during FSW/FSP still remain a subject of debate among researchers [64]. The main mechanisms involved during FSP consist of dynamic recovery (DRV), continuous dynamic recrystallization (CDRX), discontinuous dynamic recrystallization (DDRX), geometric dynamic recrystallization (GDRX), and meta-dynamic recrystallization (MDRX) [58]. DRV occurs by multiplication and interaction of dislocations in high stacking fault energy (SFE) metals such as aluminum at the initial stages of deformation, in which they rearrange and form LAGBs [64]. As the DRV mechanism progresses with more applied plastic strain, HAGBs can be formed by transformation and annihilation of LAGBs, which leads to the CDRX mechanism [65]. In DDRX, strain-free high-angle grains are formed via classical nucleation and growth [56], while the GDRX mechanism involves the impingement of elongated grain boundaries to form serrated grains [64]. MDRX implicates a continuation of DRV in the presence of stored-strain energy [64]. During FSP, materials surrounding the rotating tool during the thermo-mechanical processing experience high strains at high strain rates by a predominant simple-shear deformation mode close to the pin and shoulder center, while the temperature approach the melting point [64]. With increasing distance from the tool centerline toward the HAZ and TMAZ regions, temperature and strain gradients occur,

mainly by the influence of the shoulder. Generally for aluminum and its alloys, DRV is the dominant dynamic restoration mechanism during hot-working processes. Due to the high stacking fault energy in aluminum, climb and cross-slip of mobile dislocations can be easily achieved [58]. However, the high strain rates of the FSW/FSP processes can attain higher dislocation densities and therefore increase the chance to initiate and sustain DRX. Based on microstructural observations from the HAZ and TMAZ regions shown in Figs. 4b and 5b, the final microstructure consists of small sub-grains and elongated grains formed by high temperature plastic deformation mainly induced by the shoulder. At first, sub-grains are formed by DRV and then a continuous increase of misorientation angle progresses between sub-grains as marked by CDRX. According to the EBSD results presented in Figs. 3 to 5, the final high-angle grain structure of SZ is finer than the initial sub-grain structure of Al-Mg alloy before FSP or BM which indicate the occurrence of grain nucleation and growth mechanisms during FSP in the presence of GNPs. Regarding the DDRX mechanism, initially the dynamic nucleation occurs at the sub-grains formed by DRV, and this is followed by migration of HAGBs. During straining through the FSP process, high densities of geometrically necessary dislocations form in the presence of GNPs, which can increase the nucleation rate during DRX by accommodation of strain incompatibility. Also, clusters of GNPs (with the sizes higher than 1 μm) can act as preferred nucleation sites for formation of new grains according to the particulate-stimulated nucleation (PSN) mechanism [57, 67]. Furthermore, these incorporated nano-platelets can also pin the grain boundaries according to the Zener-Holloman mechanism [68] and therefore decrease the rate of grain boundary migration. These two mechanisms simultaneously contribute to grain refinement and the formation of a finer grain structure in the SZ of FSPed nanocomposite compared to the processed alloy metal alone.

3.4 Distribution of GNPs and phase characterizations

FE-SEM images demonstrating the grain structure of Al-matrix at the SZ of FSPed nanocomposite and distribution of precipitates in the presence of GNPs are presented in Figs. 13a to 13f. In these images, precipitates are clearly defined with the white color contrast inside the grain structure. Fig. 14 shows TEM images indicating the dispersion of the incorporated GNPs within the grain matrix and along the grain boundaries. As can be clearly observed in Figs. 14a,c-e, the GNPs introduced during FSP process, the grain boundaries are well pinned and restricted their migration in agreement with the hypothesis proposed in the previous section based on the EBSD analysis. These TEM images at different locations indicate the uniformity and dominance of the pinning effect inside the SZ. As discussed earlier [64], it is well known that the operating dynamic restoration mechanisms during severe plastic deformation of FSP process are controlled by the size and dispersion of the secondary phase inclusions. Given that the GNPs are thermally stable and insoluble in the matrix, and observed to undergo clustering to sizes higher than one micron, it is significant to find evidence for the PSN mechanism. As shown in TEM micro-graphs of Fig. 14, the reinforcing nano-platelets are dispersed homogenously within the grains and along the boundaries. The pinning effect of these randomly distributed GNPs can be estimated by considering the following Zener equation [68]:

$$P_z = \frac{3F_v\gamma_\beta}{d} \quad (1)$$

where, F_v is the volume fraction of reinforced GNPs, d is the average diameter of nano-platelets, γ_β is the energy of the Al-Mg matrix grain boundaries, and P_z is the induced pinning pressure [68]. For the system examined in this study which was processed up to five FSP cumulative passes, this pinning pressure can be estimated to be around 0.82 J/m^2 . It can be easily established from the proposed relation that this pinning force is strongly depended

on the size of dispersed reinforcements and their agglomeration during FSP process. The nano-platelets and their clusters located at the grain boundaries can suppress grain boundary diffusion more effectively (see Figs. 14a-d).

The corresponding SAED patterns from the deformed Al-matrix, complex precipitates, and incorporated GNPs are shown in Figs. 15a-d, respectively. The diffraction patterns for the metal-matrix indicate the presence of grains with the same orientations and therefore preferred crystallographic orientation. Moreover, the high magnification TEM images from the structure of dispersed GNPs within the Al-matrix at different locations inside the SZ are presented in Figs. 16a to 16i. It can be noted that the nano-platelets are preserved in their planar structure (indicating they are un-reacted with the aluminum matrix) during the high temperature plastic deformation imposed by the FSP process. This can be found by comparison of dispersed nano-platelets within the Al-matrix in Fig. 16 with the initial graphene powder in Fig. 1c which exhibits good thermal stability upon friction-stir processing.

3.5 Texture developments

The relatively high stacking fault energy of F.C.C metals such as aluminum and its alloys will have a strong influence on the operating dynamic restoration mechanisms (recovery and recrystallization) and control the resulting deformation textures [64]. EBSD inverse pole-figure grain maps from the BM, HAZ/TMAZ, and SZ regions across the FSPed Al-Mg-GNPs nanocomposite are presented in Fig. 17. The main textural characteristics for different regions are expressed in Table 1, as well. The calculated $\{100\}$, $\{110\}$, and $\{111\}$ inverse pole figures (IPFs) and pole figures (PFs) based on this EBSD analysis from BM, HAZ/TMAZ, and SZ regions are plotted in Figs. 18 and 19, respectively. As plotted in Fig. 2, the X0, Y0, and Z0 directions in the IPFs and PFs are related to the width, thickness, and length geometrical orientations of processed sample. In the SZ of processed Al-Mg alloy,

formation of a strong $\{112\} \langle 110 \rangle$ simple shear texture is pronounced due to severe plastic stirring action of the rotating tool, as shown in Figs. 18a and 19a. To compare with the ideal textures, orientation distribution functions (ODFs) in the orientation Euler angles spaces of $\phi_1=0$ to 90° and $\phi_2=0$ to 90° were derived for BM, HAZ/TMAZ, and SZ regions for the nanocomposite sample and presented in Figs. 20 to 22, respectively. The ideal cube textures can be superimposed on these ODFs for the aim of simplicity. Three-dimensional ODFs from the SZ have an indication of preferred orientations as plotted in Fig. 23. By evaluating the mentioned textural data, it can be noted that the annealed BM consists of a nearly random orientation (see Figs. 17a, 18b, 19b, and 20). Meanwhile, the recrystallized material within SZ exhibited a pronounced $\{100\} \langle 100 \rangle$ cube texture governed by the simple shear deformation induced by the rotating tool stirring action and formation of onion ring structure. This predominant cube texture lies on the A fiber with a close-packed direction of $\langle 100 \rangle$ aligned with the slip direction and a close-packed plane of $\{100\}$ aligned with the shear rotation direction (see Figs. 17c, 18d, 19d, 22, and 23). In HAZ and TMAZ regions, while formation of a strong $\{112\} \langle 110 \rangle$ simple shear texture is evident (see Figs. 17b, 18c, 19c, and 21).

The ideal B/\bar{B} shear textural components with close-packed directions aligned with the slip direction and close-packed planes normal to the slip plane can be generated within the SZ as a result of the predominant simple shear deformation mode induced by the stirring action of the rotating tool [50, 51]. Although, the presence of distributed GNPs will promote an increase in the rate of PSN, and thus decrease the intensity of preferred orientations, thus leading to a random distribution as previously reported in the work of McNelley et al. [64]. Meanwhile, the development of the preferred texture components in the HAZ and TMAZ regions can be attributed to the additional deformation associated with the shoulder along with the influence of a geometrical effect on strain within the DRV and CDRX mechanisms

[50]. The intensity of ideal simple shear texture component increases with distance from the center of SZ towards the HAZ and TMAZ regions. The same texture components are observed in the high pressure torsion (HPT) [69] and equal channel angular pressing (ECAP) [70] of aluminum alloys processed by large shear strains.

Another simple way to evaluate the strength of major texture components is by comparing the “J-index” value as calculated and reported in Table 1. A J-index of one indicates a completely random orientation, while a J-index of infinity represents a single crystal. The measured J-index values confirm the previous results with using orientation mapping analysis. The higher values associated with the HAZ/TMAZ regions indicates a stronger texture component in comparison to the random orientation in the BM and weak texture of SZ.

3.6 Mechanical properties

The key mechanical properties of the processed Al-Mg-GNPs nanocomposite are compared to the annealed and FSPed Al-Mg alloys in Table 2. It is found that the yield strength of the Al-Mg alloy improved significantly after nanocomposite fabrication, and increased from 68 up to 148.7 MPa, with the ultimate tensile strength increasing by 36%, while preserving the elongation to failure at around 68% of the annealed alloy. The four primary strengthening mechanisms which contribute to an improvement in the mechanical strength of metal-matrix nanocomposites, [71] include; (i) Orowan strengthening, (ii) grain and sub-grain boundary strengthening according to the Hall-Petch relationship, (iii) dislocation generation due to differences in the coefficient of thermal expansion between the Al-Mg matrix and the GNPs, and (iv) generation of geometrical dislocations owing to the strain mismatch between metal-matrix and nano-platelets during applied deformation. The average Vickers micro-hardness values from different regions across the FSPed alloy and nanocomposite are compared in Table 2. In both of the processed samples, the hardness increased gradually with distance from the BM towards the SZ as a result of both grain structural refinement and the

incorporation of GNPs in the case of the composite. The initial hardness value for the annealed Al-Mg alloy is about 55 Vickers, which increased up to 60 Vickers in the SZ due to grain refinement in the processed region. By introducing GNPs within the SZ during FSP, hardness increased by 53% to 84 Vickers. Also, a considerable increase in hardness at the HAZ and TMAZ regions are attributing to the formation of strong crystallographic textural components during FSP process. Therefore, the main result of using FSP process while incorporating GNPs includes controlling the restoration mechanisms, microstructural modifications, and texture evolution as well, such that an Al-matrix nanocomposite with a superior/enhanced combination of all mechanical properties can be produced.

4. Conclusions

In this study, multi-passes overlapping FSP process up to five passes on an Al-Mg alloy with pre-placed GNPs results in a homogenous dispersion of these secondary phase nano-platelets allowing fabrication of Al-matrix nanocomposites. The grain structure and crystallographic texture were examined by EBSD and TEM analysis techniques. These reinforcing GNPs can increase the number of nucleation sites by particulate-stimulated nucleation during the DDRX phenomenon imposed by processing. Also, these nano-platelets are responsible for grain boundary pinning and restrict grain growth after recrystallization. Both of these mechanisms simultaneously lead to the formation of a fine equiaxed recrystallized grain structure within the SZ with an average size of 2 μm . In the HAZ and TMAZ regions, DRV continued by partial CDRX, which was the main restoration mechanism caused mostly by heat generation and deformation imposed by the rotating tool shoulder. Differences between the fractions of recrystallized grains, HAGBs, and misorientation angles indicate these different operating dynamic restoration mechanisms at the HAZ/TMAZ and SZ regions, as well. Also, it was found that the fraction of CSL boundaries increases after employing the FSP process along with incorporation of GNPs. Generation of different crystallographic textures within the processed zone across the FSPed nanocomposite corresponded to the dominant shear deformation modes induced by the rotating tool.

As a result, the recrystallized SZ material exhibited a dominant cube texture component. In HAZ and TMAZ regions, the preferred orientation was strongly closed to the simple ideal shear component attributing to the local grain boundaries migration by strain state and simple-shear deformation at these regions. The FSP process allowed fabrication of a graphene reinforced Al-matrix nanocomposite stirred zone with yield strength of 150 MPa, indentation hardness of 84 Vickers, and elongation of 20%.

Acknowledgement

This work was also supported by Slovak Foundation VEGA grant 2_0158_16, and by grant APVV-14-0936. The authors wish to thank Dr. Lubomir Orovcik (Institute of Materials and Machine Mechanics, Slovak Academy of Sciences, Dúbravská cesta 9/6319, 845 13, Bratislava, Slovak Republic) for helping in RBEI imaging.

References

- [1] F. He, Q. Han, M.J. Jackson, Nanoparticulate reinforced metal matrix nanocomposites – a review, *Int. J. Nanoparticles*. 1(4) (2008) 301-309.
- [2] M. Easton, D. Stjohn, Grain refinement of aluminum alloys: Part I. The nucleant and solute paradigms - a review of the literature, *Metall. Mater. Trans. A* 30(6) (1999) 1613-1623.
- [3] J.C. Benedyk, 3 - Aluminum alloys for lightweight automotive structures A2 - Mallick, P.K, Materials, Design and Manufacturing for Lightweight Vehicles, Woodhead Publishing 2010, pp. 79-113.
- [4] L.F. Mondolfo, 8 - Technological Properties, Aluminum Alloys, Butterworth-Heinemann 1976, pp. 173-210.
- [5] G.S. Cole, A.M. Sherman, Light weight materials for automotive applications, *Mater. Charact.* 35(1) (1995) 3-9.
- [6] C. Suryanarayana, Mechanical alloying and milling, *Prog. Mater Sci.* 46(1–2) (2001) 1-184.
- [7] C. Suryanarayana, N. Al-Aqeeli, Mechanically alloyed nanocomposites, *Prog. Mater Sci.* 58(4) (2013) 383-502.
- [8] F. He, 6 - Ceramic nanoparticles in metal matrix composites*, Ceramic Nanocomposites, Woodhead Publishing 2013, pp. 185-207.
- [9] F. Khodabakhshi, A. Simchi, The role of microstructural features on the electrical resistivity and mechanical properties of powder metallurgy Al-SiC-Al₂O₃ nanocomposites, *Mater. Des.* 130 (2017) 26-36.
- [10] E.A.M. Shalaby, A.Y. Churyumov, A.N. Solonin, A. Lotfy, Preparation and characterization of hybrid A359/(SiC+Si₃N₄) composites synthesized by stir/squeeze casting techniques, *Mater. Sci. Eng., A* 674 (2016) 18-24.

- [11] M. Shamanian, M. Mohammadnezhad, J. Szpunar, Texture analysis of a friction stir welded ultrafine grained Al–Al₂O₃ composite produced by accumulative roll-bonding, *J. Alloys Compd.* 615 (2014) 651-656.
- [12] R.S. Mishra, Z.Y. Ma, I. Charit, Friction stir processing: a novel technique for fabrication of surface composite, *Mater. Sci. Eng., A* 341(1–2) (2003) 307-310.
- [13] F. Khodabakhshi, A. Simchi, A.H. Kokabi, Surface modifications of an aluminum-magnesium alloy through reactive stir friction processing with titanium oxide nanoparticles for enhanced sliding wear resistance, *Surf. Coat. Technol.* 309 (2017) 114-123.
- [14] V. Sharma, U. Prakash, B.V.M. Kumar, Surface composites by friction stir processing: A review, *J. Mater. Process. Technol.* 224 (2015) 117-134.
- [15] R.S. Mishra, Z.Y. Ma, Friction stir welding and processing, *Mater. Sci. Eng., R* 50(1–2) (2005) 1-78.
- [16] R. Nandan, T. DebRoy, H.K.D.H. Bhadeshia, Recent advances in friction-stir welding – Process, weldment structure and properties, *Prog. Mater Sci.* 53(6) (2008) 980-1023.
- [17] A. Simar, Y. Bréchet, B. de Meester, A. Denquin, C. Gallais, T. Pardoen, Integrated modeling of friction stir welding of 6xxx series Al alloys: Process, microstructure and properties, *Prog. Mater Sci.* 57(1) (2012) 95-183.
- [18] D.R. Ni, D.L. Chen, D. Wang, B.L. Xiao, Z.Y. Ma, Influence of microstructural evolution on tensile properties of friction stir welded joint of rolled SiCp/AA2009-T351 sheet, *Mater. Des.* 51 (2013) 199-205.
- [19] F. Khodabakhshi, A.P. Gerlich, P. Švec, Fabrication of a high strength ultra-fine grained Al-Mg-SiC nanocomposite by multi-step friction-stir processing, *Mater. Sci. Eng., A* 698 (2017) 313-325.
- [20] F. Khodabakhshi, A. Simchi, A.H. Kokabi, A.P. Gerlich, Similar and dissimilar friction-stir welding of an PM aluminum-matrix hybrid nanocomposite and commercial pure

aluminum: Microstructure and mechanical properties, *Mater. Sci. Eng., A* 666 (2016) 225-237.

[21] M. Ashjari, A. Mostafapour Asl, S. Rouhi, Experimental investigation on the effect of process environment on the mechanical properties of AA5083/Al₂O₃ nanocomposite fabricated via friction stir processing, *Mater. Sci. Eng., A* 645 (2015) 40-46.

[22] F. Khodabakhshi, H. Ghasemi Yazdabadi, A.H. Kokabi, A. Simchi, Friction stir welding of a P/M Al–Al₂O₃ nanocomposite: Microstructure and mechanical properties, *Mater. Sci. Eng., A* 585 (2013) 222-232.

[23] F. Khodabakhshi, A. Simchi, A.H. Kokabi, A.P. Gerlich, M. Nosko, P. Švec, Influence of hard inclusions on microstructural characteristics and textural components during dissimilar friction-stir welding of an PM Al–Al₂O₃–SiC hybrid nanocomposite with AA1050 alloy, *Sci. Technol. Weld. Joining* 22(5) (2017) 412-427.

[24] M. Narimani, B. Lotfi, Z. Sadeghian, Evaluation of the microstructure and wear behaviour of AA6063-B₄C/TiB₂ mono and hybrid composite layers produced by friction stir processing, *Surf. Coat. Technol.* 285 (2016) 1-10.

[25] N. Yuvaraj, S. Aravindan, Vipin, Fabrication of Al5083/B₄C surface composite by friction stir processing and its tribological characterization, *J. Mater. Res. Technol.* 4(4) (2015) 398-410.

[26] C.M. Rejil, I. Dinaharan, S.J. Vijay, N. Murugan, Microstructure and sliding wear behavior of AA6360/(TiC + B₄C) hybrid surface composite layer synthesized by friction stir processing on aluminum substrate, *Mater. Sci. Eng., A* 552 (2012) 336-344.

[27] Y. Morisada, H. Fujii, T. Nagaoka, K. Nogi, M. Fukusumi, Fullerene/A5083 composites fabricated by material flow during friction stir processing, *Composites Part A*. 38(10) (2007) 2097-2101.

[28] S. Ramesh, A. Sivasamy, K.Y. Rhee, S.J. Park, D. Hui, Preparation and characterization

of maleimide–polystyrene/SiO₂–Al₂O₃ hybrid nanocomposites by an *in situ* sol–gel process and its antimicrobial activity, *Composites Part B*. 75 (2015) 167-175.

[29] G.L. You, N.J. Ho, P.W. Kao, *In-situ* formation of Al₂O₃ nanoparticles during friction stir processing of Al-SiO₂ composite, *Mater. Charact.* 80 (2013) 1-8.

[30] F. Khodabakhshi, A.P. Gerlich, A. Simchi, A.H. Kokabi, Hot deformation behavior of an aluminum-matrix hybrid nanocomposite fabricated by friction stir processing, *Mater. Sci. Eng., A* 626 (2015) 458-466.

[31] F. Khodabakhshi, A.P. Gerlich, A. Simchi, A.H. Kokabi, Cryogenic friction-stir processing of ultrafine-grained Al–Mg–TiO₂ nanocomposites, *Mater. Sci. Eng., A* 620 (2015) 471-482.

[32] F. Khodabakhshi, A. Simchi, A.H. Kokabi, M. Sadeghahmadi, A.P. Gerlich, Reactive friction stir processing of AA 5052–TiO₂ nanocomposite: process–microstructure–mechanical characteristics, *Mater. Sci. Technol.* 31(4) (2015) 426-435.

[33] H. Eskandari, R. Taheri, F. Khodabakhshi, Friction-stir processing of an AA8026-TiB₂-Al₂O₃ hybrid nanocomposite: Microstructural developments and mechanical properties, *Mater. Sci. Eng., A* 660 (2016) 84-96.

[34] F. Khodabakhshi, A. Simchi, A.H. Kokabi, A.P. Gerlich, Friction stir processing of an aluminum-magnesium alloy with pre-placing elemental titanium powder: *In-situ* formation of an Al₃Ti-reinforced nanocomposite and materials characterization, *Mater. Charact.* 108 (2015) 102-114.

[35] Z.Y. Liu, B.L. Xiao, W.G. Wang, Z.Y. Ma, Singly dispersed carbon nanotube/aluminum composites fabricated by powder metallurgy combined with friction stir processing, *Carbon* 50(5) (2012) 1843-1852.

[36] W.J. Kim, T.J. Lee, S.H. Han, Multi-layer graphene/copper composites: Preparation using high-ratio differential speed rolling, microstructure and mechanical properties, *Carbon*

69 (2014) 55-65.

[37] K. Kondoh, H. Fukuda, J. Umeda, H. Imai, B. Fugetsu, Microstructural and mechanical behavior of multi-walled carbon nanotubes reinforced Al–Mg–Si alloy composites in aging treatment, *Carbon* 72 (2014) 15-21.

[38] S. Stankovich, D.A. Dikin, G.H.B. Dommett, K.M. Kohlhaas, E.J. Zimney, E.A. Stach, R.D. Piner, S.T. Nguyen, R.S. Ruoff, Graphene-based composite materials, *Nature* 442(7100) (2006) 282-286.

[39] M. Tachibana, S. Yamada, Two-dimensional nanocarbon materials called carbon nanowalls—Structure, physical properties and applications, *Carbon* 55 (2013) 373-374.

[40] Z. Hu, X. Lu, Chapter 8 - Mechanical Properties of Carbon Nanotubes and Graphene A2 - Tanaka, K, in: S. Iijima (Ed.), *Carbon Nanotubes and Graphene* (Second Edition), Elsevier, Oxford, 2014, pp. 165-200.

[41] A. Dorri Moghadam, E. Omrani, P.L. Menezes, P.K. Rohatgi, Mechanical and tribological properties of self-lubricating metal matrix nanocomposites reinforced by carbon nanotubes (CNTs) and graphene – A review, *Composites Part B*. 77 (2015) 402-420.

[42] S. Feng, Q. Guo, Z. Li, G. Fan, Z. Li, D.B. Xiong, Y. Su, Z. Tan, J. Zhang, D. Zhang, Strengthening and toughening mechanisms in graphene-Al nanolaminated composite micro-pillars, *Acta Mater.* 125 (2017) 98-108.

[43] A. Nieto, A. Bisht, D. Lahiri, C. Zhang, A. Agarwal, Graphene reinforced metal and ceramic matrix composites: a review, *Int. Mater. Rev.* (2016) 1-62.

[44] H.G.P. Kumar, M.A. Xavior, Graphene Reinforced Metal Matrix Composite (GRMMC): A Review, *Procedia Eng.* 97 (2014) 1033-1040.

[45] H.G. Prashantha Kumar, M. Anthony Xavior, Graphene reinforced metal matrix composite (GRMMC): A review, *Procedia Eng.* 2014, pp. 1033-1040.

[46] M. Rashad, F. Pan, A. Tang, M. Asif, Effect of Graphene Nanoplatelets addition on

mechanical properties of pure aluminum using a semi-powder method, *Prog. Nat. Sci.* 24(2) (2014) 101-108.

[47] S.F. Bartolucci, J. Paras, M.A. Rafiee, J. Rafiee, S. Lee, D. Kapoor, N. Koratkar,

Graphene–aluminum nanocomposites, *Mater. Sci. Eng., A* 528(27) (2011) 7933-7937.

[48] L.Y. Chen, H. Konishi, A. Fehrenbacher, C. Ma, J.Q. Xu, H. Choi, H.F. Xu, F.E.

Pfefferkorn, X.C. Li, Novel nanoprocessing route for bulk graphene nanoplatelets reinforced metal matrix nanocomposites, *Scripta Mater.* 67(1) (2012) 29-32.

[49] C.H. Jeon, Y.H. Jeong, J.J. Seo, H.N. Tien, S.T. Hong, Y.J. Yum, S.H. Hur, K.J. Lee,

Material properties of graphene/aluminum metal matrix composites fabricated by friction stir processing, *Int. J. Precis. Eng. Manuf.* 15(6) (2014) 1235-1239.

[50] R.W. Fonda, K.E. Knipling, Texture development in friction stir welds, *Sci. Technol.*

Weld. Joining 16(4) (2011) 288-294.

[51] U.F.H.R. Suhuddin, S. Mironov, Y.S. Sato, H. Kokawa, Grain structure and texture

evolution during friction stir welding of thin 6016 aluminum alloy sheets, *Mater. Sci. Eng., A* 527(7–8) (2010) 1962-1969.

[52] N. Yasavol, A. Abdollah-zadeh, M.T. Vieira, H.R. Jafarian, Microstructure evolution

and texture development in a friction stir-processed AISI D2 tool steel, *Appl. Surf. Sci.* 293 (2014) 151-159.

[53] B. Wang, B.B. Lei, J.X. Zhu, Q. Feng, L. Wang, D. Wu, EBSD study on microstructure

and texture of friction stir welded AA5052-O and AA6061-T6 dissimilar joint, *Mater. Des.* 87 (2015) 593-599.

[54] M.M.Z. Ahmed, B.P. Wynne, W.M. Rainforth, P.L. Threadgill, Microstructure,

crystallographic texture and mechanical properties of friction stir welded AA2017A, *Mater. Charact.* 64 (2012) 107-117.

[55] M. Abbasi, T.W. Nelson, C.D. Sorensen, Transformation and Deformation Texture

Study in Friction Stir Processed API X80 Pipeline Steel, *Metall. Mater. Trans. A* 43(13) (2012) 4940-4946.

[56] F. Khodabakhshi, A. Simchi, A.H. Kokabi, A.P. Gerlich, M. Nosko, Effects of stored strain energy on restoration mechanisms and texture components in an aluminum–magnesium alloy prepared by friction stir processing, *Mater. Sci. Eng., A* 642 (2015) 204-214.

[57] F. Khodabakhshi, A. Simchi, A.H. Kokabi, M. Nosko, F. Simančík, P. Švec, Microstructure and texture development during friction stir processing of Al–Mg alloy sheets with TiO₂ nanoparticles, *Mater. Sci. Eng., A* 605 (2014) 108-118.

[58] T. Sakai, A. Belyakov, R. Kaibyshev, H. Miura, J.J. Jonas, Dynamic and post-dynamic recrystallization under hot, cold and severe plastic deformation conditions, *Prog. Mater. Sci.* 60 (2014) 130-207.

[59] Y. Cao, H. Di, J. Zhang, J. Zhang, T. Ma, R.D.K. Misra, An electron backscattered diffraction study on the dynamic recrystallization behavior of a nickel–chromium alloy (800H) during hot deformation, *Mater. Sci. Eng., A* 585 (2013) 71-85.

[60] M. Shamanian, H. Mostaan, M. Safari, J.A. Szpunar, EBSD Study on Grain Boundary and Microtexture Evolutions During Friction Stir Processing of A413 Cast Aluminum Alloy, *J. Mater. Eng. Perform.* 25(7) (2016) 2824-2835.

[61] ASTM standard E8M. Tension testing of metallic materials. Annual Book of ASTM Standards; ASTM, West Conshohocken; 03.01.1998.

[62] ASTM standard E384-99. Standard Test Method for Microindentation Hardness of Materials. Annual Book of ASTM Standards; ASTM, West Conshohocken; 03.01.1999.

[63] J.Q. Su, T.W. Nelson, C.J. Sterling, Microstructure evolution during FSW/FSP of high strength aluminum alloys, *Mater. Sci. Eng., A* 405(1–2) (2005) 277-286.

[64] T.R. McNelley, S. Swaminathan, J.Q. Su, Recrystallization mechanisms during friction stir welding/processing of aluminum alloys, *Scripta Mater.* 58(5) (2008) 349-354.

- [65] K.V. Jata, S.L. Semiatin, Continuous dynamic recrystallization during friction stir welding of high strength aluminum alloys, *Scripta Mater.* 43(8) (2000) 743-749.
- [66] A.L. Etter, T. Baudin, N. Fredj, R. Penelle, Recrystallization mechanisms in 5251 H14 and 5251-O aluminum friction stir welds, *Mater. Sci. Eng., A* 445–446 (2007) 94-99.
- [67] F. Khodabakhshi, A. Simchi, A.H. Kokabi, P. Švec, F. Simančík, A.P. Gerlich, Effects of nanometric inclusions on the microstructural characteristics and strengthening of a friction-stir processed aluminum–magnesium alloy, *Mater. Sci. Eng., A* 642 (2015) 215-229.
- [68] A.H. Ammouri, G. Kridli, G. Ayoub, R.F. Hamade, Relating grain size to the Zener–Hollomon parameter for twin-roll-cast AZ31B alloy refined by friction stir processing, *J. Mater. Process. Technol.* 222 (2015) 301-306.
- [69] S. Naghdy, L. Kestens, S. Hertelé, P. Verleysen, Evolution of microstructure and texture in commercial pure aluminum subjected to high pressure torsion processing, *Mater. Charact.* 120 (2016) 285-294.
- [70] C. Lu, G.Y. Deng, A.K. Tieu, L.H. Su, H.T. Zhu, X.H. Liu, Crystal plasticity modeling of texture evolution and heterogeneity in equal channel angular pressing of aluminum single crystal, *Acta Mater.* 59(9) (2011) 3581-3592.
- [71] Z. Zhang, D.L. Chen, Consideration of Orowan strengthening effect in particulate-reinforced metal matrix nanocomposites: A model for predicting their yield strength, *Scripta Mater.* 54(7) (2006) 1321-1326.

Figure Captions

Figure 1. (a-c) TEM images and (d) diffraction pattern from GNPs.

Figure 2. Stereographic macro-image from the thickness cross section of the FSPed (a) Al-Mg alloy and (b) Al-Mg-GNPs nanocomposite.

Figure 3. FE-SEM macro-structure from the BM, HAZ, TMAZ, and SZ regions across the processed nanocomposite.

Figure 4. EBSD grain boundary maps from the (a) SZ of FSPed Al-Mg alloy, (b) BM, (c) HAZ/TMAZ, and (d) SZ of the nanocomposite sample.

Figure 5. EBSD orientation maps measured in the (a) BM, (b) HAZ/TMAZ, and (c) SZ regions of the processed nanocomposite.

Figure 6. Grain size distribution histograms for the (a) BM, (b) HAZ/TMAZ, and (c) SZ regions across the FSPed nanocomposite.

Figure 7. EBSD recrystallization maps measured in the (a) BM, (b) HAZ/TMAZ, and (c) SZ regions of the processed nanocomposite.

Figure 8. Frequency of recrystallized, substructured, and deformed grain boundaries within the (a) BM, (b) HAZ/TMAZ, and (c) SZ regions of the FSPed nanocomposite.

Figure 9. The superimposed positions of coincident site lattice (CSL) boundaries on the pattern quality maps for the (a) BM, (b) HAZ/TMAZ, and (c) SZ regions of the processed nanocomposite.

Figure 10. Histograms of CSL boundaries frequency versus Sigma-value for the (a) BM, (b) HAZ/TMAZ, and (c) SZ regions across the FSPed nanocomposite.

Figure 11. (a-c, f, h) Bright- and (d-e, g, i) dark-field TEM images from the grain structure of SZ at different regions and different magnifications for the processed nanocomposite sample.

Figure 12. (a) Selected area diffraction pattern and (b) image from a recrystallized grain within the SZ of processed nanocomposite.

Figure 13. FE-SEM images from the distribution of precipitates (white contrast) within the grain structure of Al-matrix in the SZ of processed nanocomposite at different magnifications of (a) $\times 250$, (b) $\times 500$, (c) $\times 1000$, (d) $\times 2000$, (e) $\times 3500$, and (f) $\times 5000$.

Figure 14. Distribution of GNPs within the grains and along the grain boundaries for the SZ of FSPed nanocomposite at different locations and different magnifications; (a, c-f) Bright- and (b) dark-fields TEM images.

Figure 15. Diffraction spot patterns combined with related TEM images from the (a) deformed Al-matrix structure, (b, c) precipitates, and (d) cluster of GNPs.

Figure 16. High-magnification TEM images representing the structure of dispersed GNPs at different regions and different magnifications; (a, c-i) Bright- and (b) dark-fields TEM images.

Figure 17. EBSD inverse pole-figure maps from the (a) BM, (b) HAZ/TMAZ, and (c) SZ of the nanocomposite sample.

Figure 18. Inverse pole-figure (IPF) maps demonstrating the dominant orientations for the (a) SZ of FSPed Al-Mg alloy, (b) BM, (c) HAZ/TMAZ, and (d) SZ regions across the FSPed nanocomposite.

Figure 19. The $\{100\}$, $\{110\}$, and $\{111\}$ pole figures (PFs) for the (a) SZ of FSPed Al-Mg alloy, (b) BM, (c) HAZ/TMAZ, and (d) SZ regions of the processed nanocomposite.

Figure 20. Orientation distribution function (ODF) for the BM.

Figure 21. Orientation distribution function (ODF) for the HAZ and TMAZ regions.

Figure 22. Orientation distribution function (ODF) for the SZ of processed nanocomposite.

Figure 23. 3D ODF plots representing the dominant textural components within the SZ; (a) S, (b), Q (c), (110) cubic, and (d) all.

Table 1. Main microstructural characteristics for different regions across the FSPed Al-Mg alloy and Al-Mg-GNPs nanocomposite.

Zone	Fraction of grains (%)			Mean grain size (μm)	Fraction of HAGBs (%)	Mean misorientation angle (degree)	Fraction of low Σ CSL boundaries (%)	J-index
	Recrystallized	Substructured	Deformed					
BM	96.1	2.4	1.5	10.7	89.4	30.1	4.02	1.1
HAZ/TMAZ	75.2	23.3	1.5	9.7	89.9	30.5	6.42	6.2
SZ-Alloy	93.4	5.4	1.3	4.5	91.2	30.7	4.3	1.7
SZ-Nanocomposite	90.2	9.0	0.8	2.1	93.0	31.2	2.96	2.8

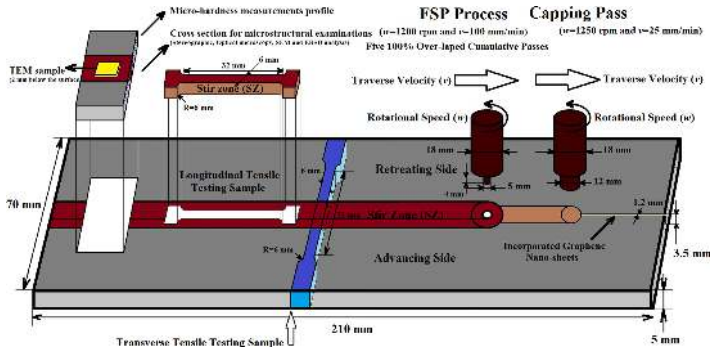
Table 2. Main mechanical properties of the processed alloy and nanocomposite samples: σ_y : Yield stress; σ_{UTS} : Ultimate tensile strength; σ_f :

Fracture stress; e : Elongation to failure; HV : Mean Vickers indentation hardness

Material	Tensile properties				Indentation hardness (Vickers)			
	$\sigma_y (MPa)$	$\sigma_{UTS} (MPa)$	$\sigma_f (MPa)$	$e(\%)$	BM	HAZ	TMAZ	SZ
Annealed Al-Mg alloy	68	180	159	29.5	55±0.9	-	-	-
FSPed Al-Mg alloy	70	206	174	28.5	55±0.9	55±0.9	57.8±1.2	60±2.0
FSPed Al-Mg-GNPs nanocomposite	148.7	244.3	89.1	20.1	55±0.9	55±0.9	64.3±3.1	84±2.2

Highlights:

- A new Al-matrix nanocomposite was prepared by friction stir processing.
- Improved hardness and strength were attained by incorporation of graphene nano-platelets.
- Microstructural changes, restoration mechanisms and textural developments were studied.
- The correlation between the microstructural features and textural components was established.



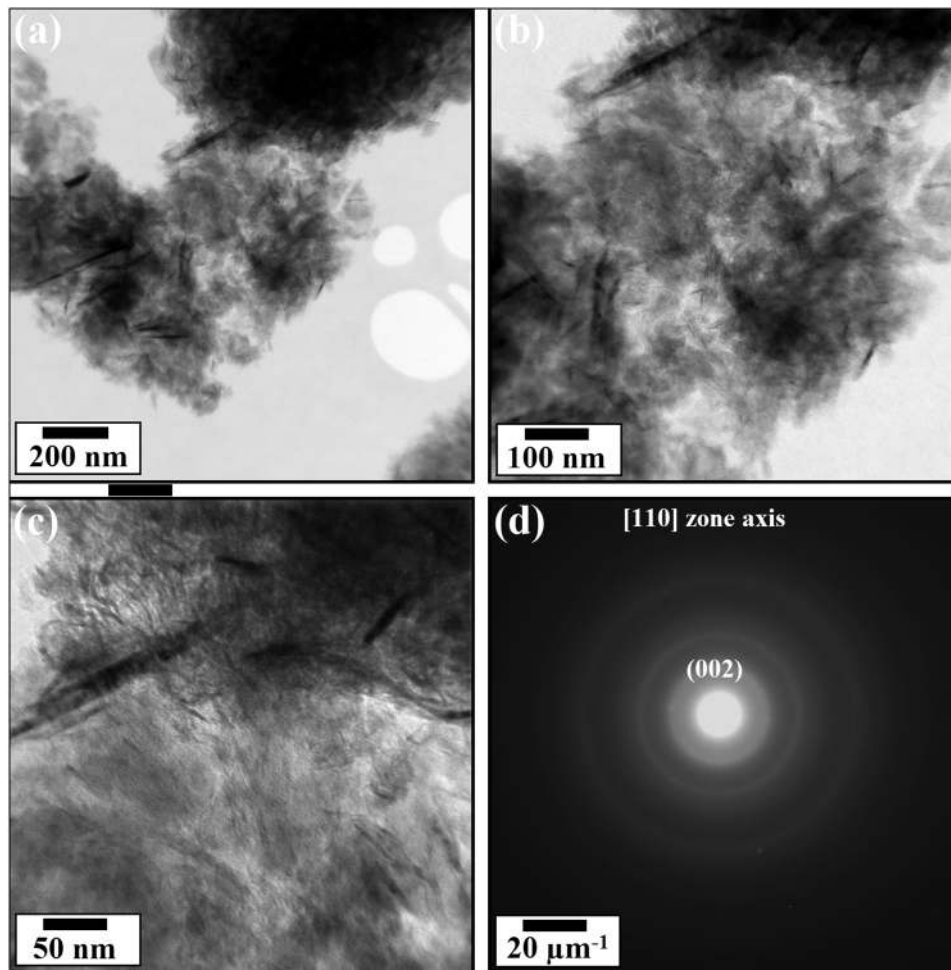


Figure 1

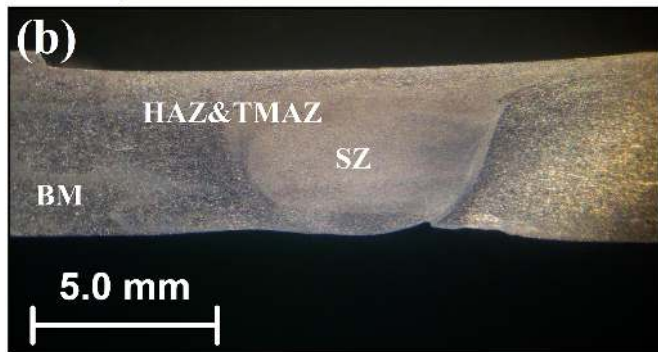
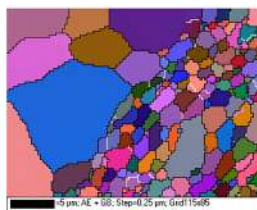
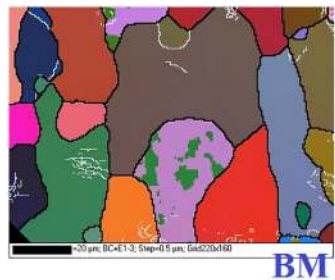
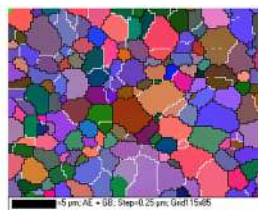


Figure 2



HAZ-TMAZ



SZ

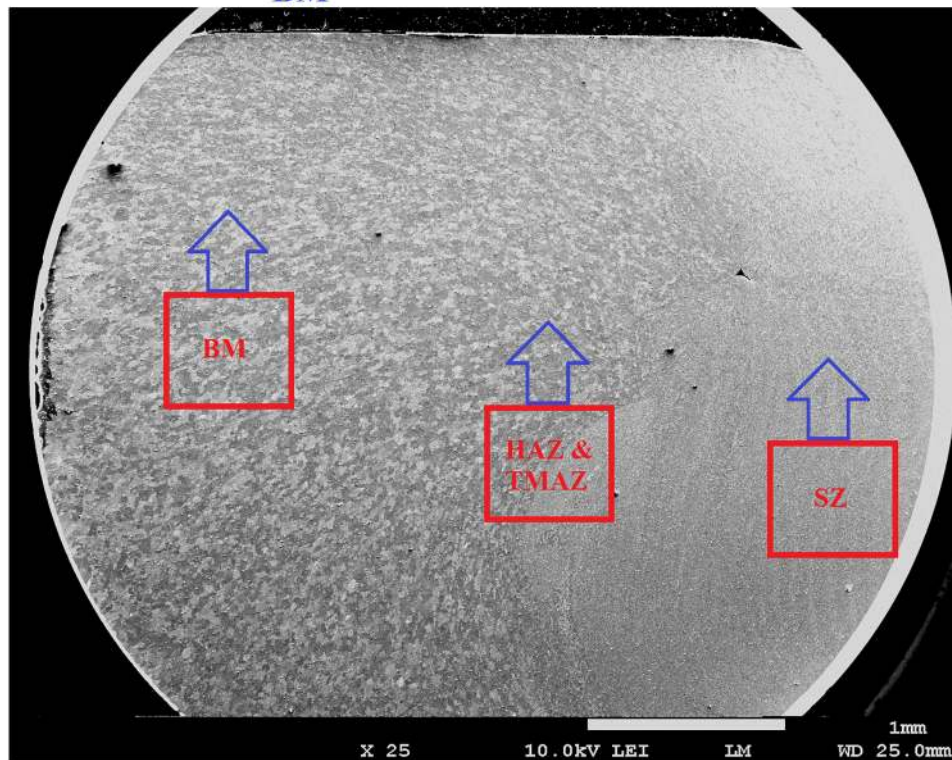


Figure 3

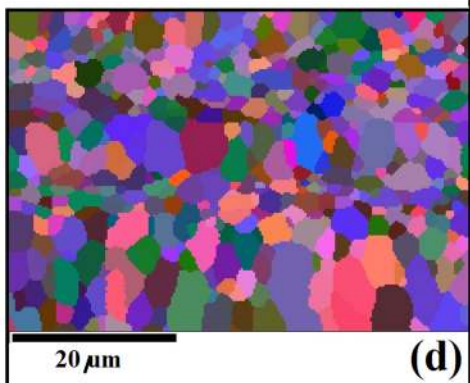
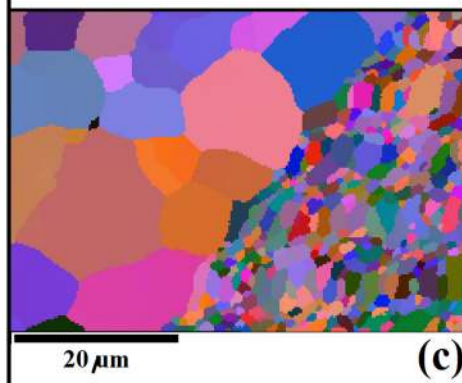
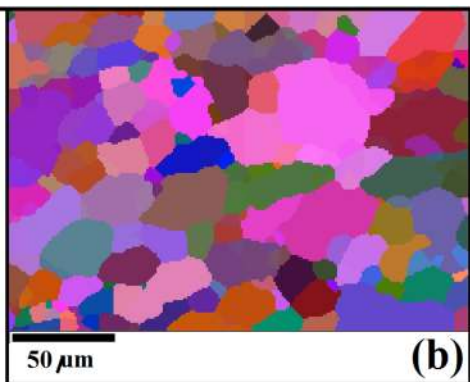
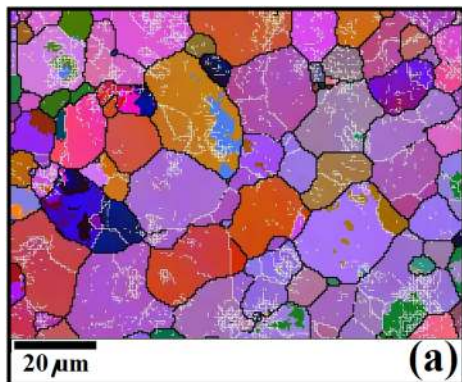


Figure 4

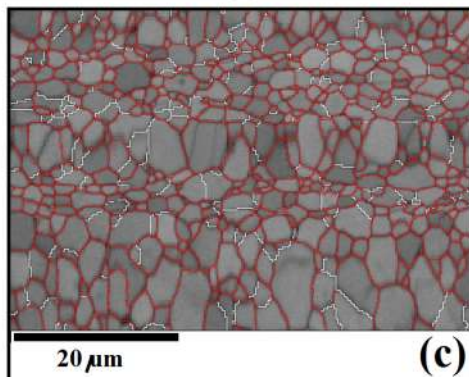
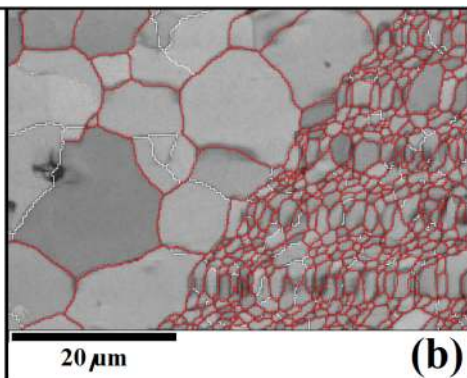
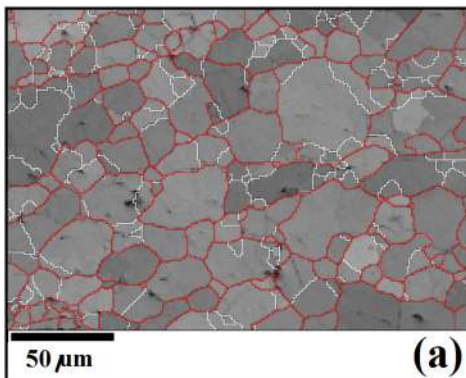


Figure 5

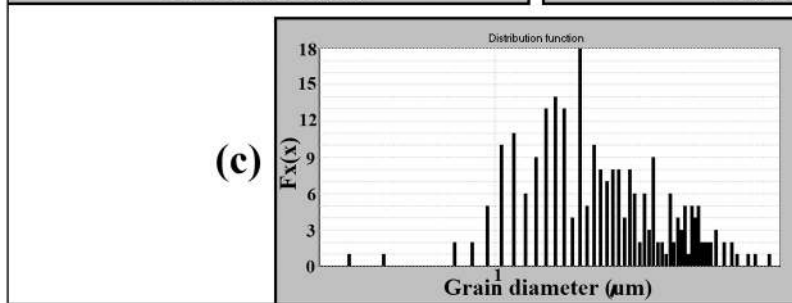
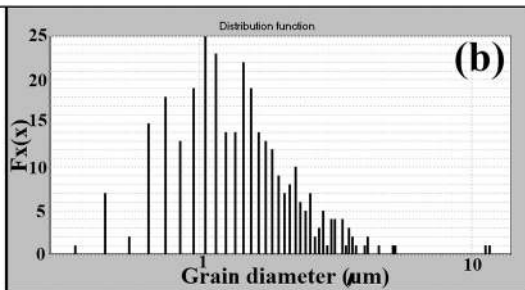
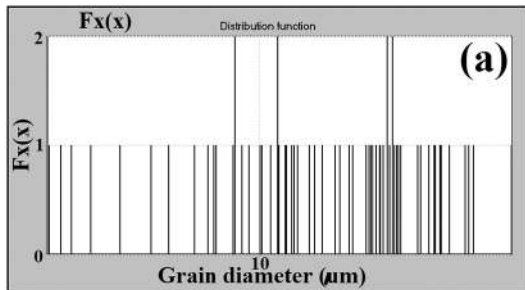


Figure 6

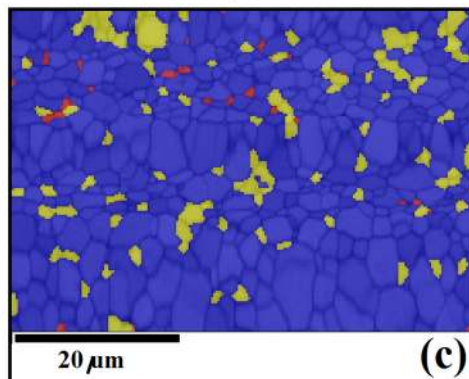
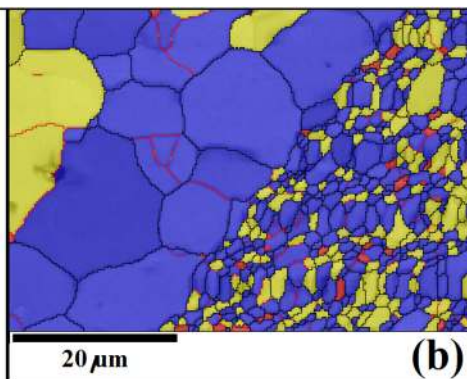
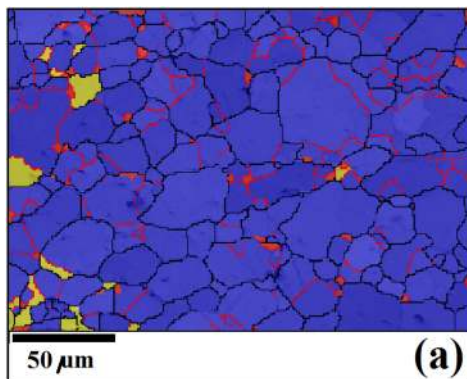


Figure 7

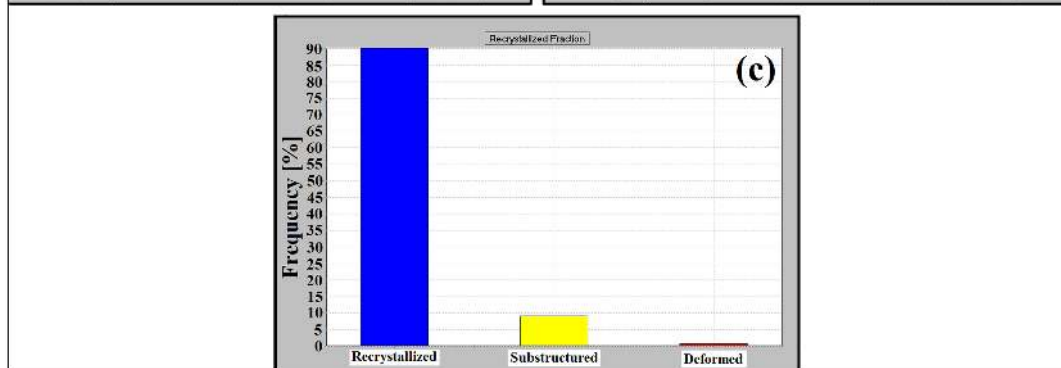
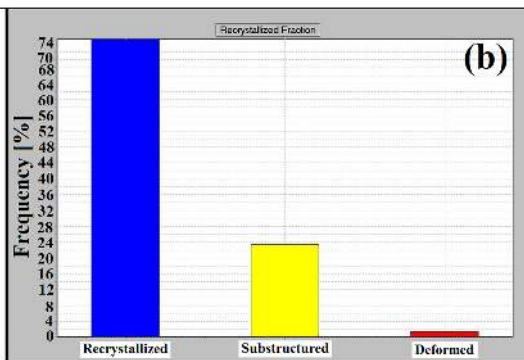
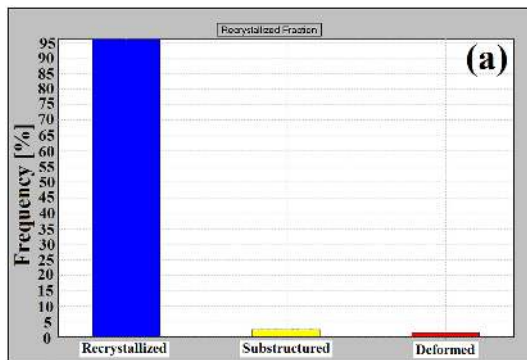


Figure 8

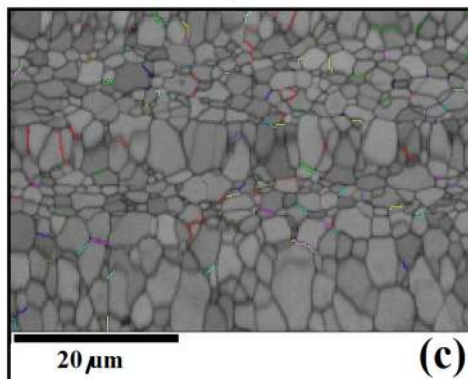
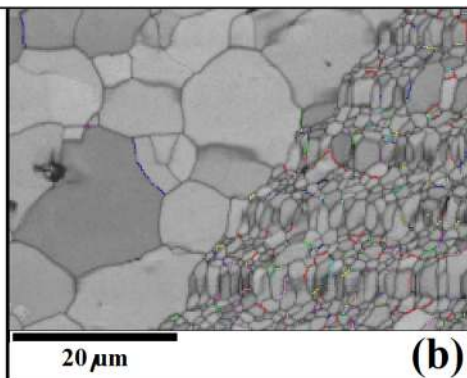
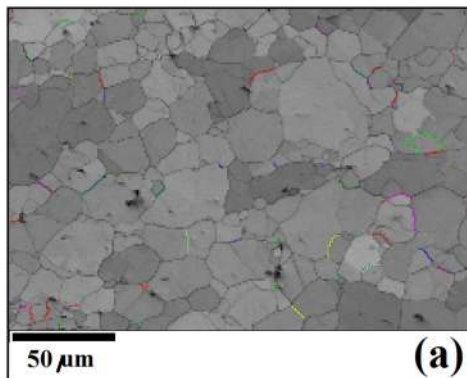


Figure 9

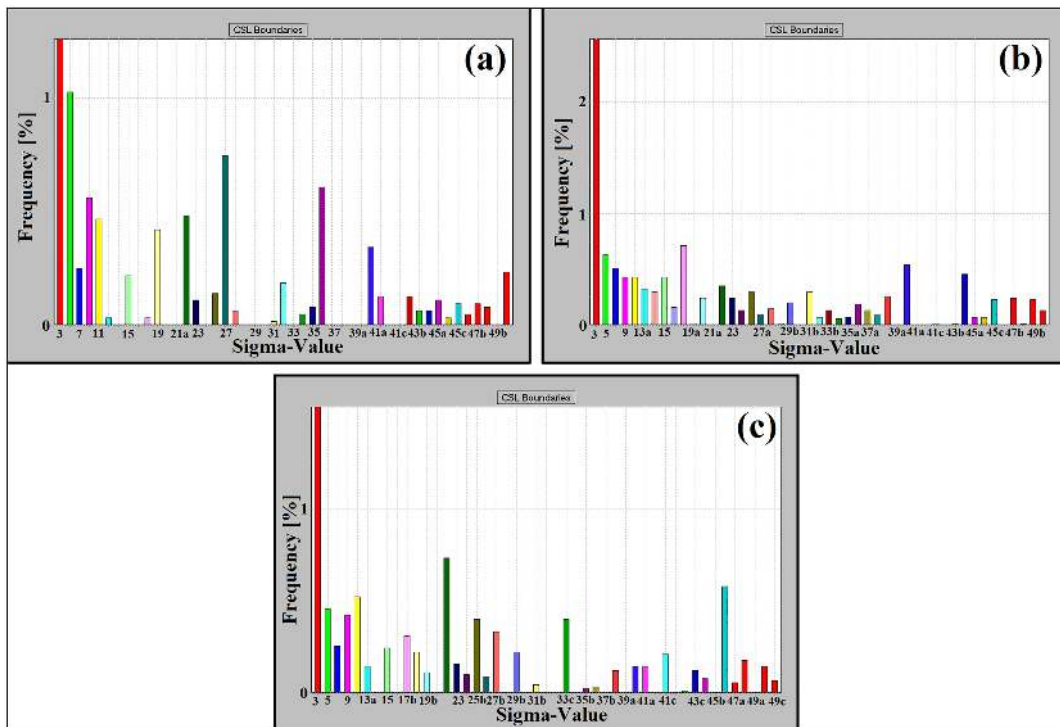


Figure 10

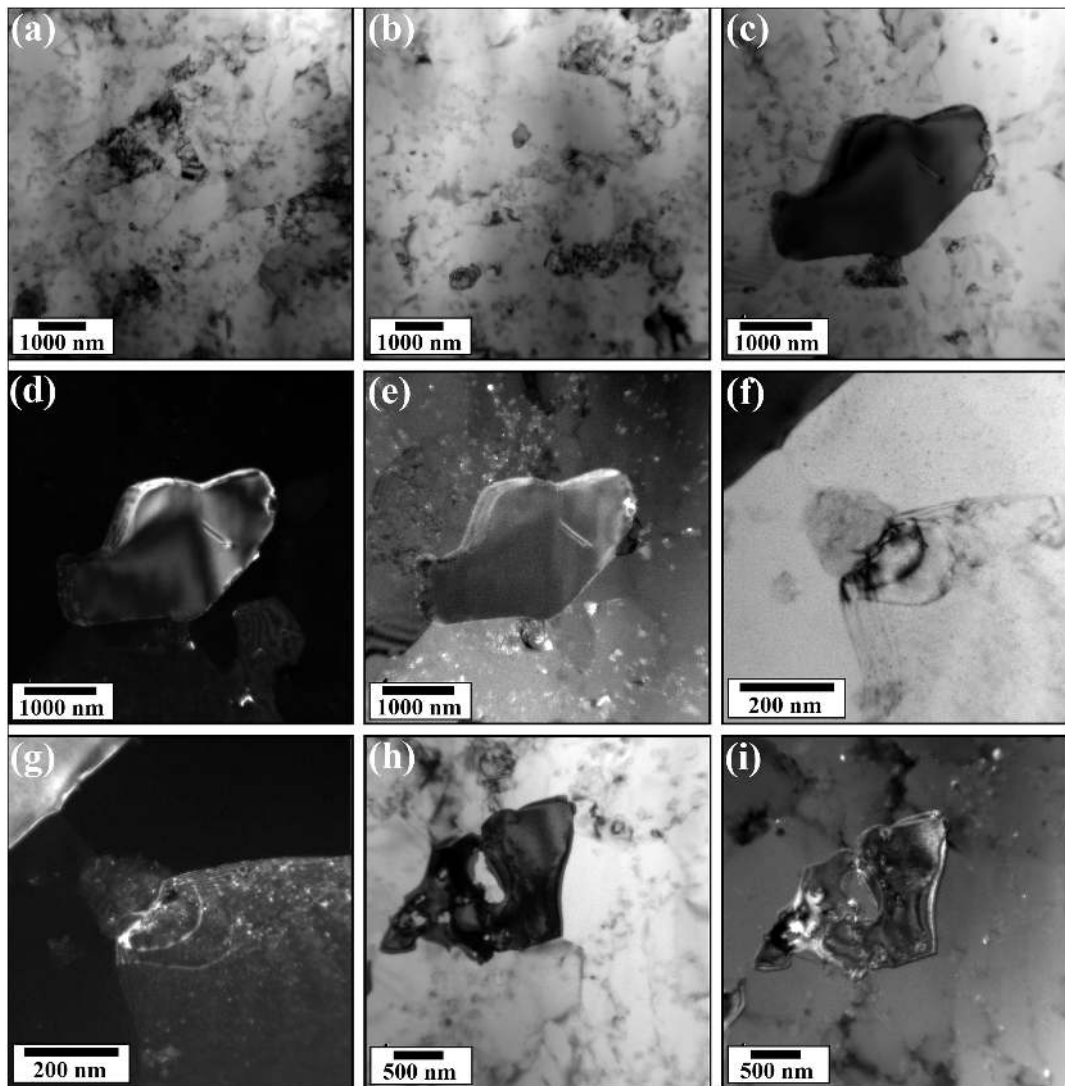


Figure 11

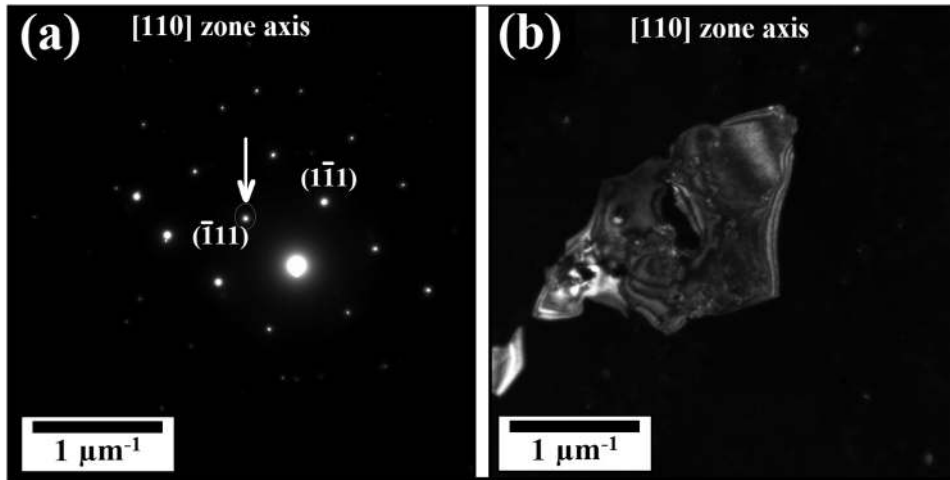


Figure 12

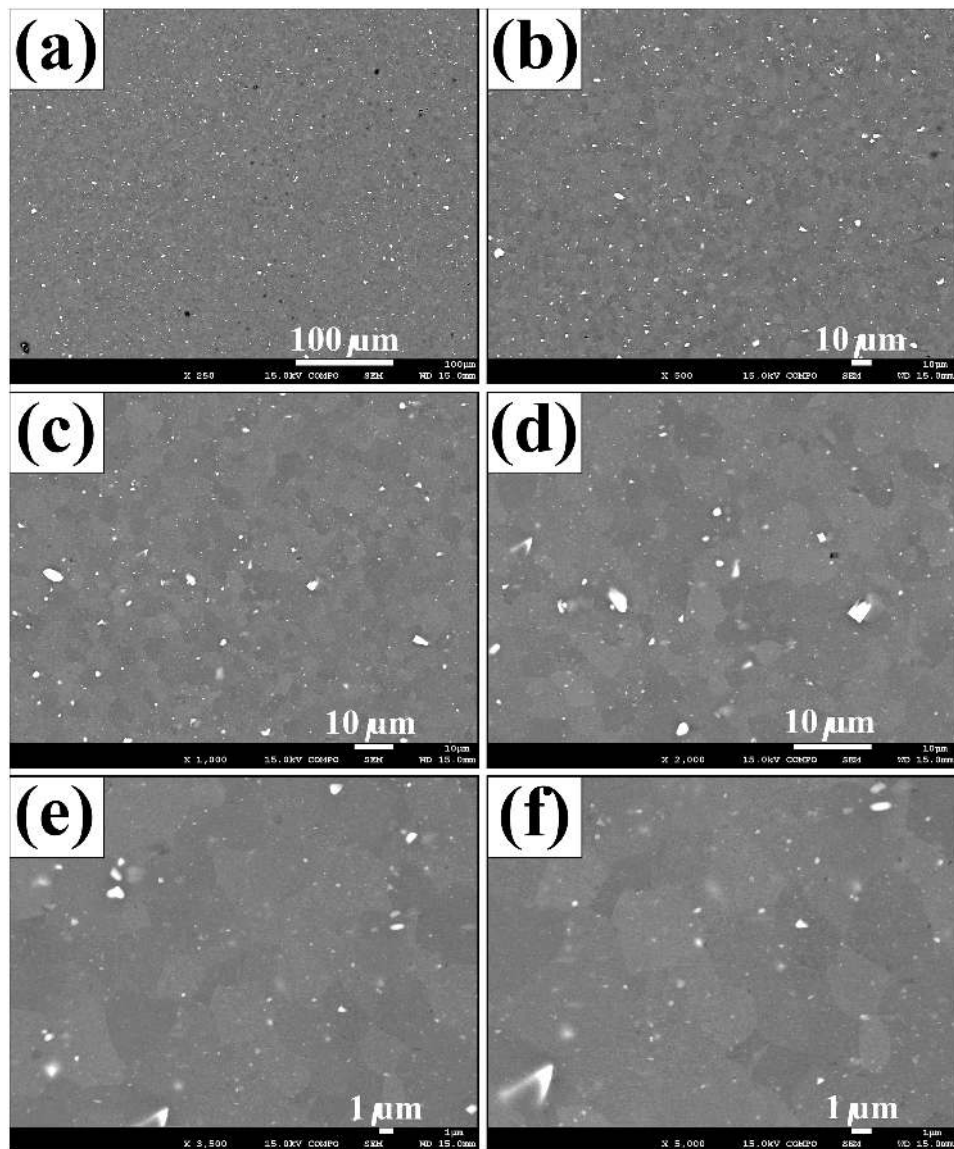


Figure 13

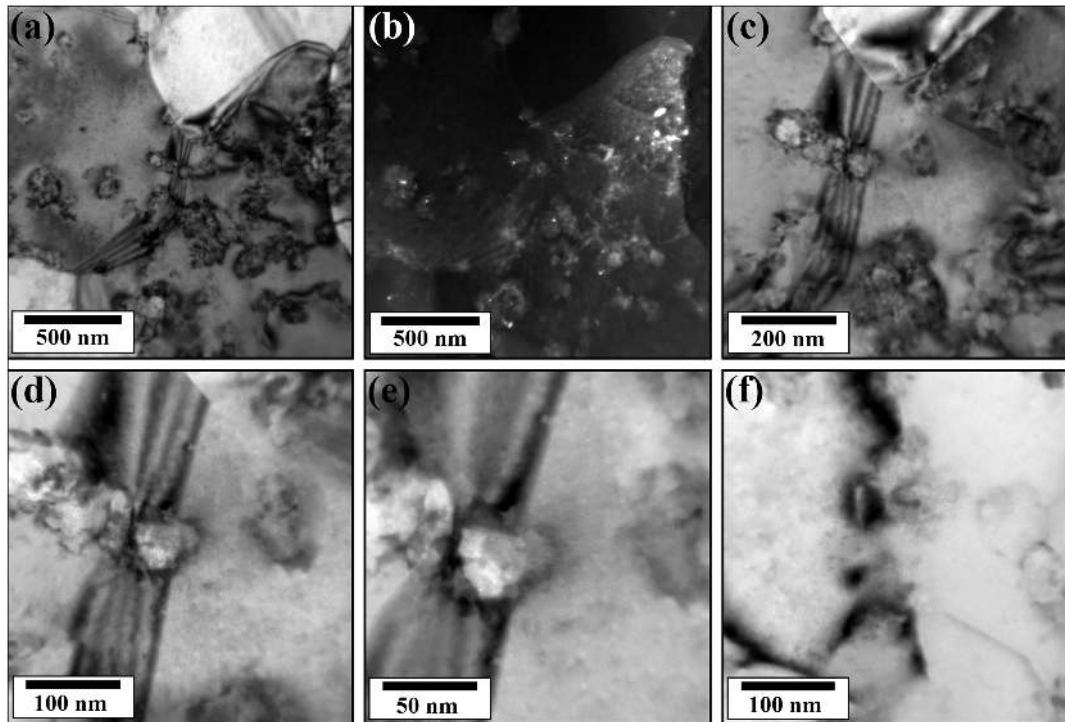


Figure 14

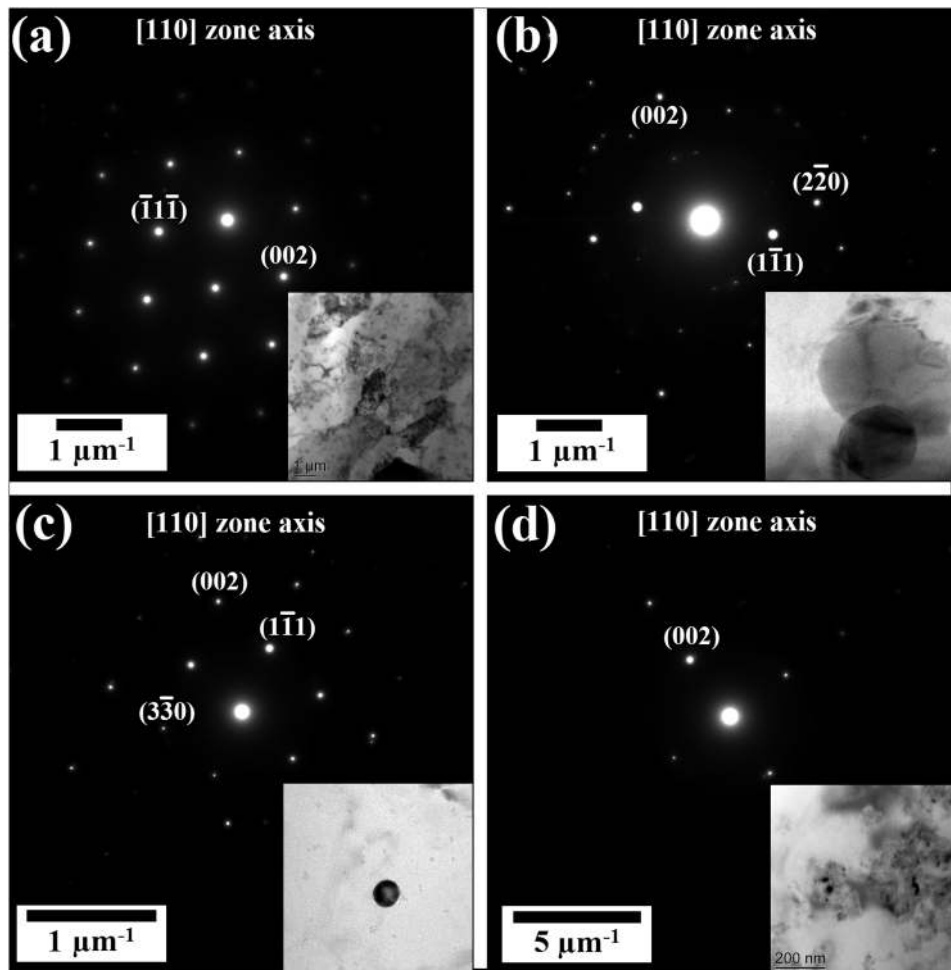


Figure 15

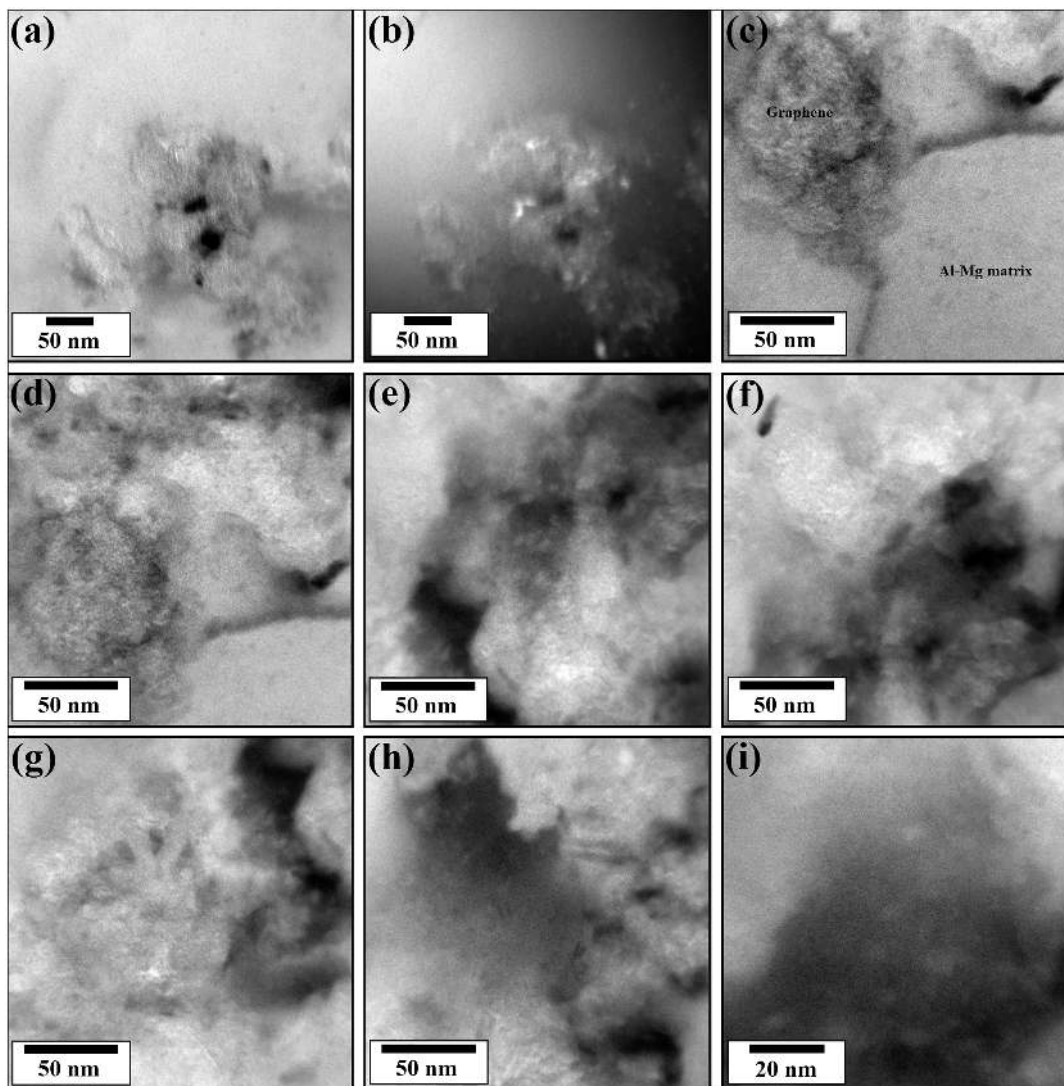


Figure 16

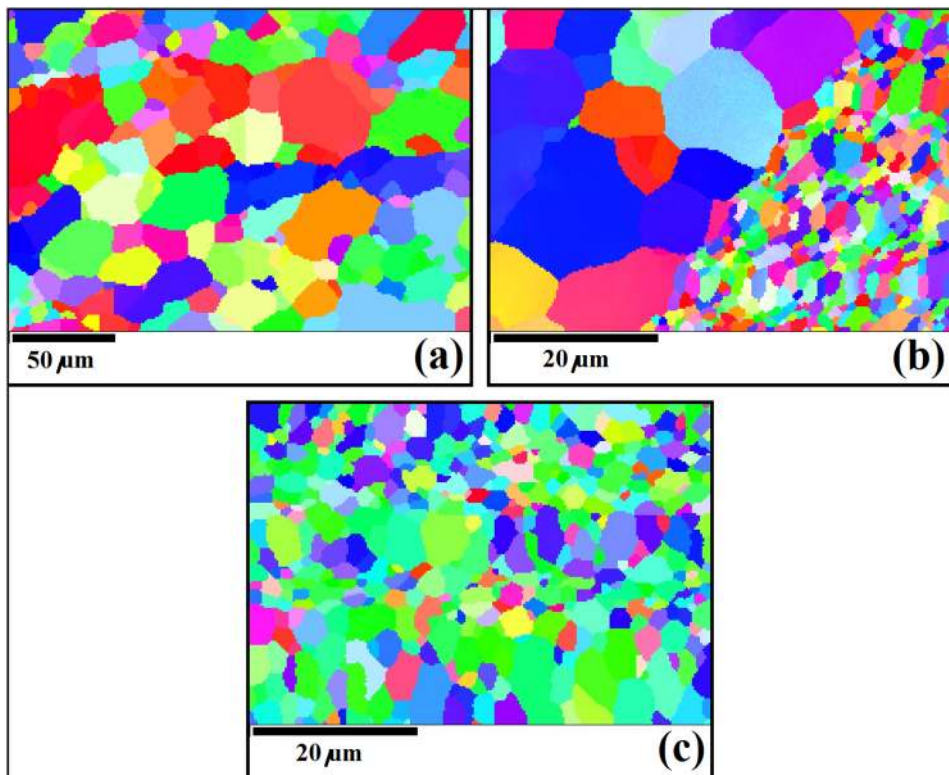


Figure 17

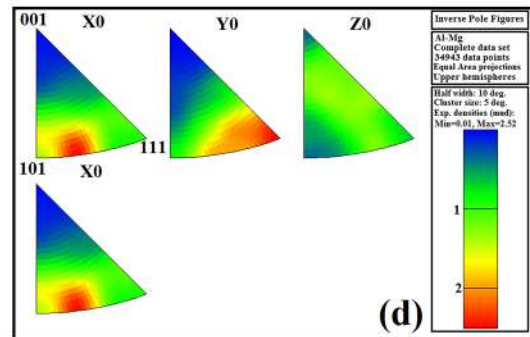
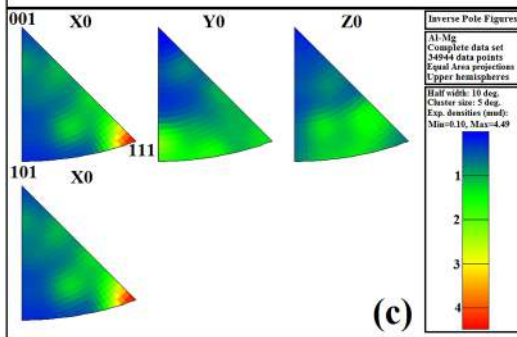
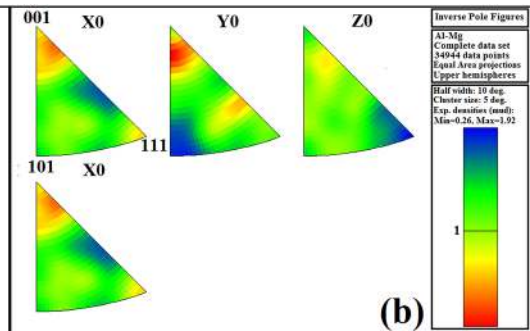
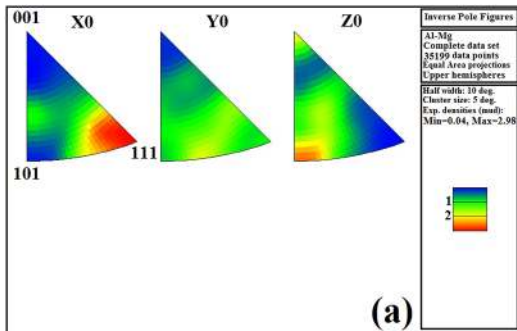


Figure 18

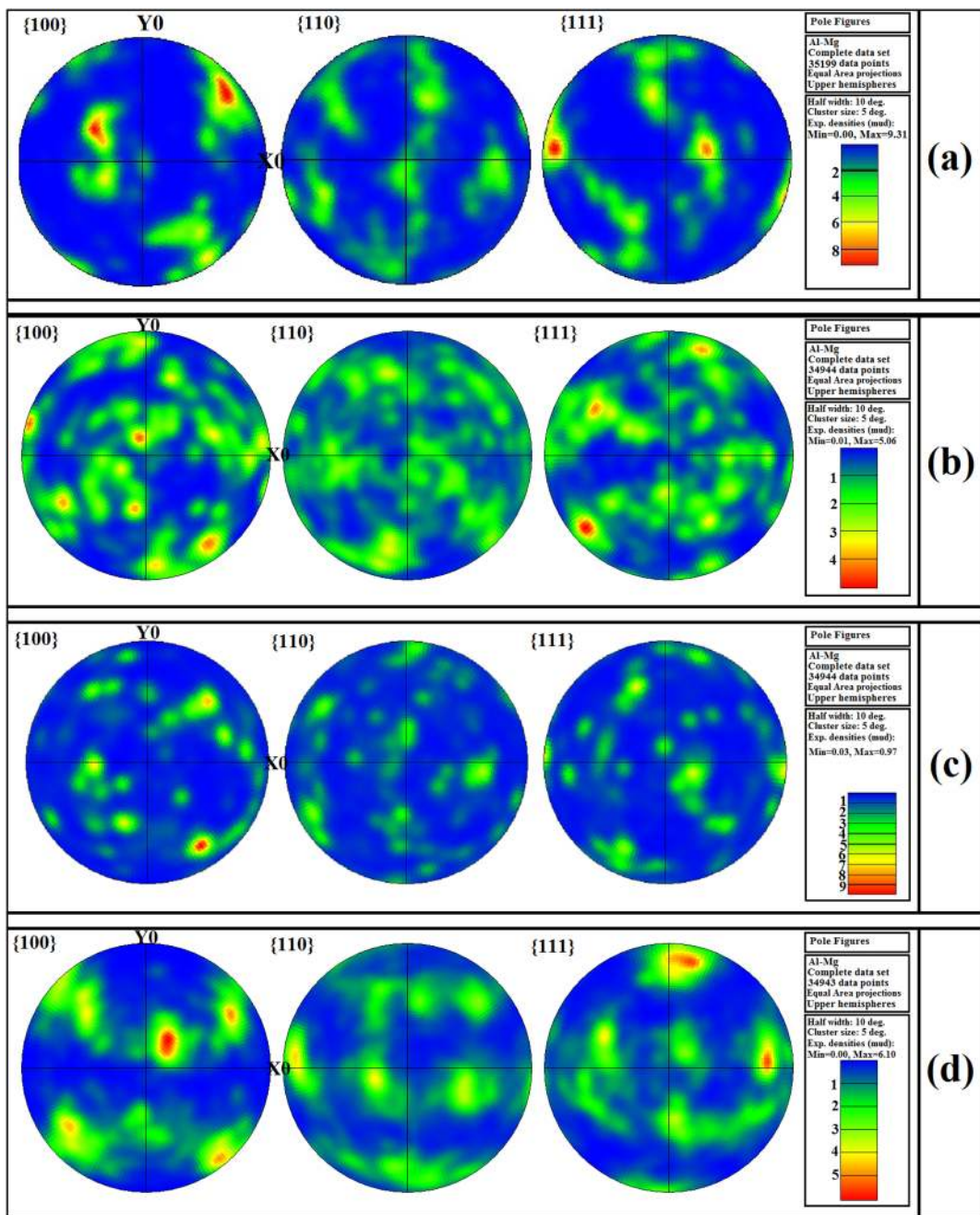


Figure 19

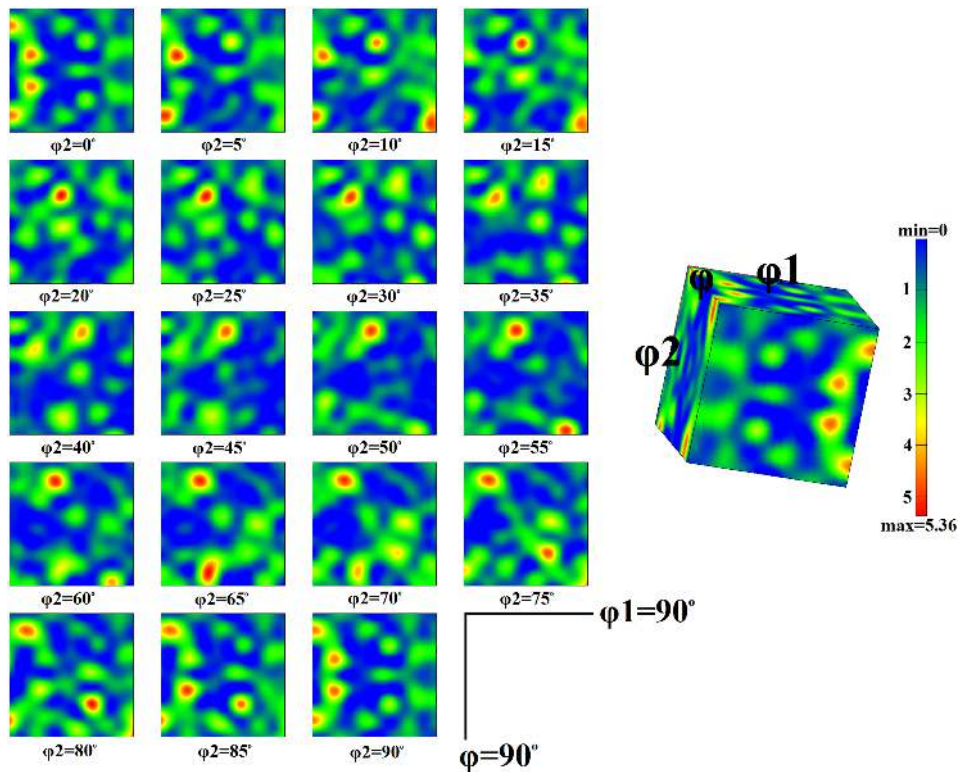


Figure 20

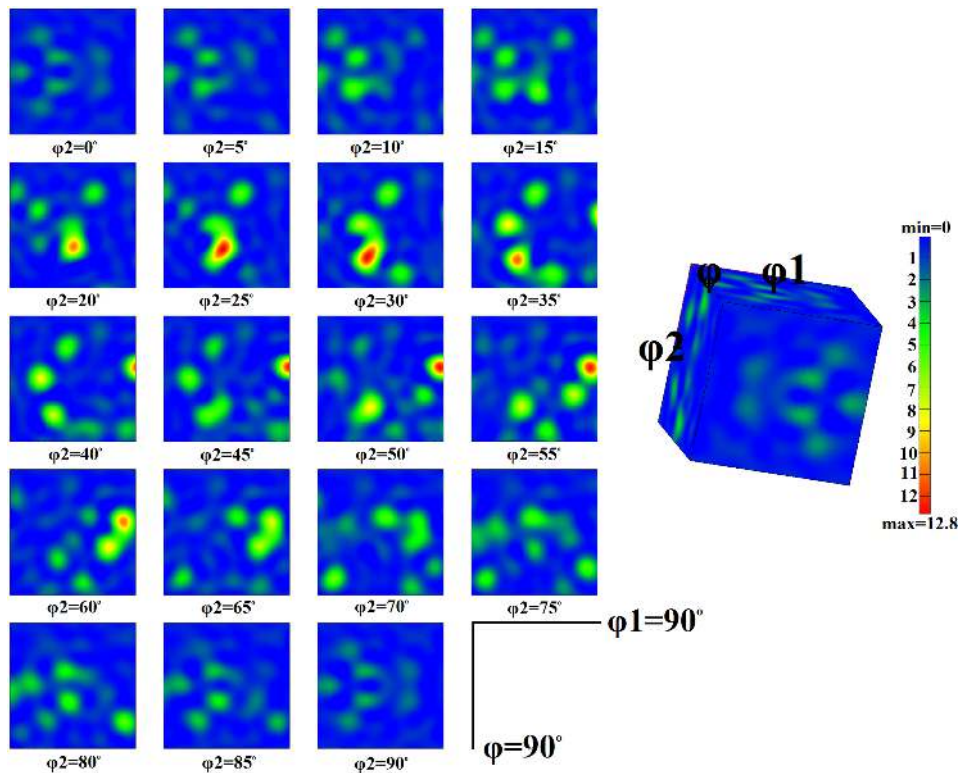


Figure 21

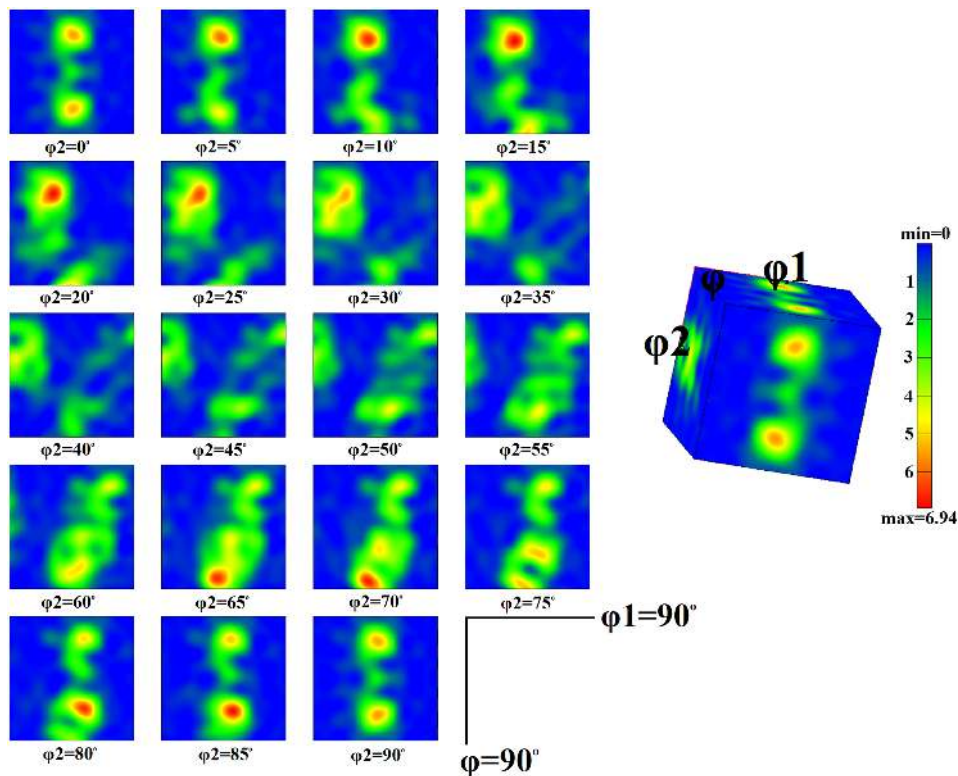


Figure 22

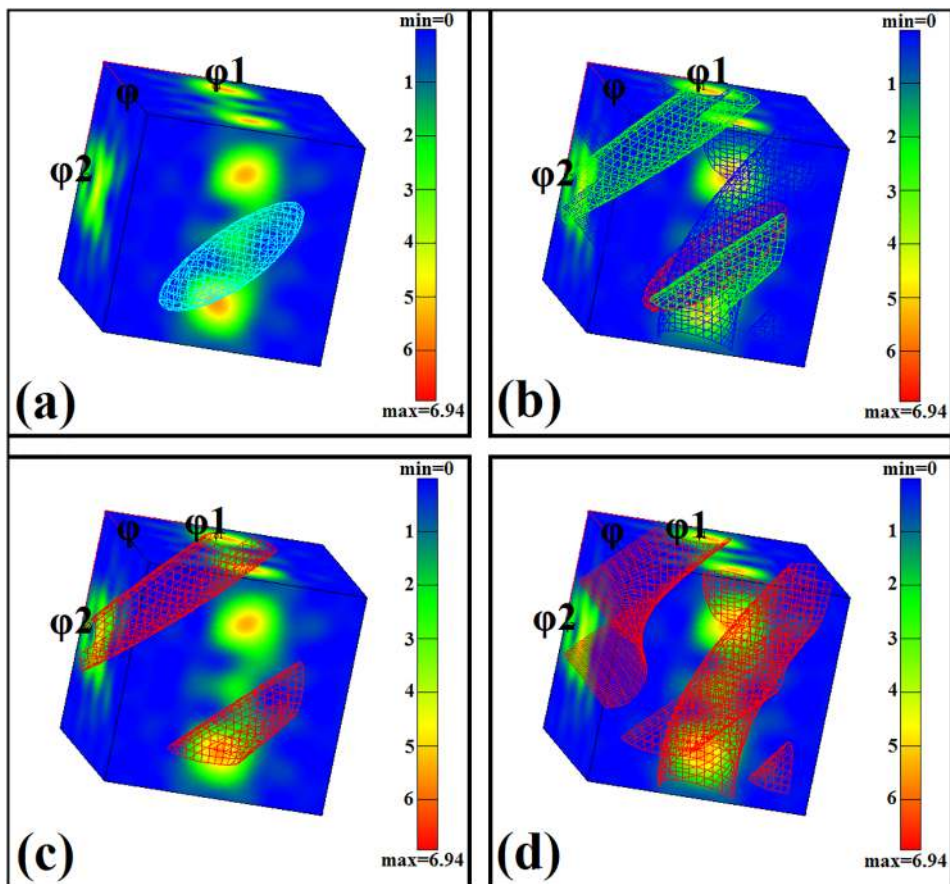


Figure 23